

Aerosol Retrievals from the Multiyear Multisatellite AVHRR Pathfinder Atmosphere (PATMOS) Dataset for Correcting Remotely Sensed Sea Surface Temperatures

ALEXANDER IGNATOV* AND NICHOLAS R. NALLI*

NOAA/NESDIS, Office of Research and Applications, Camp Springs, Maryland

(Manuscript received 25 January 2002, in final form 11 July 2002)

ABSTRACT

Eight-year (1990–98), two-satellite (*NOAA-11* and *-14*), global daily $\sim(110 \text{ km})^2$ gridded observations from the Advanced Very High Resolution Radiometer (AVHRR) Pathfinder Atmosphere (PATMOS) dataset have been previously merged with the Pathfinder Matchup Database (PFMDB) and used to develop the Phase I aerosol correction for sea surface temperatures (SSTs) from AVHRR. In this study, this unique PATMOS–BUOY matchup dataset ($N = 105\,831$) is used to derive and quality control an advanced set of aerosol parameters to be used in the Phase II algorithm: aerosol optical depths in channels 1 ($\lambda_1 = 0.63 \mu\text{m}$) and 2 ($\lambda_2 = 0.83 \mu\text{m}$), τ_1 and τ_2 , and Ångström exponent $\alpha = -\ln(\tau_1/\tau_2)/\ln(\lambda_1/\lambda_2)$. Inaccurate retrievals at low sun and outliers are removed from the data. PATMOS global, multiyear, multisatellite aerosol properties, derived from cloud-free portions of the $(110 \text{ km})^2$ grid, resemble many features previously observed in the space–time-restricted, $(8 \text{ km})^2$ resolution Aerosol Observation (AEROBS) operational retrievals, in spite of a different spatial resolution, cloud screening, and sampling. Histograms of τ and α are accurately fit by lognormal and normal probability density functions, respectively. Retrievals of τ_2 are consistent with τ_1 at low τ , but reveal high multiplicative bias, resulting in a low additive bias in α . Random errors in α are inversely proportional to τ , with signal-to-noise ratio well approximated as $\eta = \tau_1/\tau_{10}$. Parameter τ_{10} (τ threshold at which signal in α compares to its noise, i.e., $\eta = 1$) in PATMOS data ($\tau_{10} \sim 0.11 \pm 0.01$) is less than in AEROBS ($\tau_{10} \sim 0.18 \pm 0.02$), since noise is suppressed by the additional spatial averaging in PATMOS. The effect of cloud screening and sampling is also quantified. PATMOS τ_1 , τ_2 , and α reveal a strong trend against cloud amount, which is not fully understood, and some residual artificial time/angle trends, due to undercorrected calibration errors and remaining algorithm problems. But overall, they show a high degree of self- and interconsistency, thus providing a superior set of aerosol predictors to be used in the Phase II SST aerosol correction algorithm.

1. Introduction

The Advanced Very High Resolution Radiometer (AVHRR/2) on board the National Oceanic and Atmospheric Administration (NOAA) polar orbiting satellites measures upward radiance in five spectral channels, centered at ~ 0.63 , 0.83 , 3.7 , 11 , and $12 \mu\text{m}$ (Kidwell 1995). Of these, the two longwave infrared *emission* channels (4–5) are used for retrievals of sea surface temperature (SST; Nalli and Stowe 2002, and references therein), whereas the two shortwave *reflectance* channels (1–2) are used for aerosol retrievals (Ignatov and Stowe 2002a,b and references therein). Aerosols are known to cause systematic errors in SST retrievals. A project was initiated at NOAA to develop an aerosol

correction to SST using synergetic aerosol retrievals from the same sensor (Nalli and Stowe 2002).

A global 8-yr PATMOS–BUOY dataset ($N = 105\,831$ observations) was specially created for this project by merging the NOAA–National Aeronautics and Space Administration (NASA) Pathfinder Atmosphere (PATMOS) data from *NOAA-11* (January 1990–December 1993) and *-14* (January 1995–December 1998) satellites with the Pathfinder Matchup Data Base (PFMDB; Nalli and Stowe 2002). (Note a 1-yr gap resulting from loss of *NOAA-13* on 21 August 1993. *NOAA-13* was launched on 9 August 1993 to replace the then-operational *NOAA-11*.) PATMOS provides $(110 \text{ km})^2$ statistics [mean and standard deviation of Global Area Coverage (GAC) pixels, calculated separately for the clear-sky and cloudy fractions of each grid] of AVHRR radiances, surface geography, and observation–illumination geometry, along with retrievals made therefrom (Stowe et al. 2002). PFMDB is a global database of in situ observations by moored and drifting buoys matched-up with NOAA satellite overpasses from 1985 to 1998 (Kilpatrick et al. 2001). The unique PATMOS–BUOY dataset retains all the parameters available from the merged datasets. In partic-

* CIRA Visiting Scientists.

Corresponding author address: Dr. Alexander Ignatov, NOAA/NESDIS, E/RA1, Rm. 712, WWBG, 5200 Auth Road, Camp Springs, MD 20746-4304.
E-mail: alex.ignatov@noaa.gov

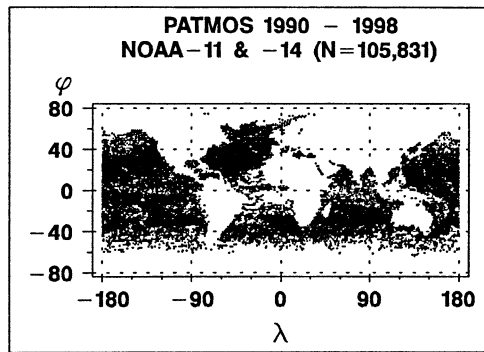


FIG. 1. Geographical coverage by the PATMOS-BUOY data.

ular, PATMOS provides cloud amount, A_T (a fraction of cloudy GAC pixels within a PATMOS grid cell), and PFMDB occasionally contributes measurements of surface wind speed and integral water vapor, thus allowing unique empirical checks of aerosol retrievals.

In Phase I of the project documented by Nalli and Stowe (2002), the aerosol correction is estimated from two predictors, those being the aerosol optical depth (AOD) in channel 1, τ_1 , derived with an earlier algorithm (Stowe et al. 1997), and a ratio of clear-sky channel 1 and 2 reflectances, ρ_1/ρ_2 (used as a proxy for aerosol particle size). The primary objective of this paper is to retrieve, analyze, and quality ensure an advanced (more accurate τ_1) and extended (newly derived AOD in channel 2, τ_2 , and Ångström exponent, α) set of aerosol parameters from the PATMOS-BUOY dataset for use in deriving a Phase II aerosol SST correction algorithm to be documented in a companion paper (Nalli and Ignatov 2002, unpublished manuscript).

Previous analyses from NOAA-14 operational Aerosol Observations (AEROBS) datasets (four periods each covering 9–14 days from February 1998 to May 1999), collected over the 5°–25°S global latitudinal belt, have been limited in space and time (Ignatov and Stowe 2002b). Thus, a secondary objective of our PATMOS-based analyses is to provide a far more comprehensive global (see geographical coverage of matchups in Fig. 1), multiyear, multisatellite perspective, along with additional analyses that include the effect of cloud screening and sampling on aerosol retrievals.

In this paper, retrievals of τ_1 and τ_2 are made independently from channels 1 and 2 using satellite-specific lookup tables (LUTs) derived from the 6S-radiative transfer model (RTM; Vermote et al. 1997). The NOAA-14 LUTs have been tested previously with AEROBS operational data (Ignatov and Stowe 2002a). The 6S-based retrievals of τ_1 are compared against the Dave-RTM-based AOD distributed with PATMOS, τ_{ID} . The difference $\delta\tau_1 = \tau_{ID} - \tau_1 \sim -3.5 \times 10^{-2}$ is partially due to the use of more accurate, satellite-specific LUTs in the retrievals, but primarily results from the incorrectly specified input to the Dave-based LUT1 used in PATMOS. These findings are documented in section 2.

The remaining sections in the paper are dedicated to analyses based upon the more accurate and versatile 6S-RTM based, satellite-specific retrievals. In section 3, τ_1 and τ_2 are quality-controlled (QC). Retrievals at high solar zenith angles ($\theta_o > 60^\circ$) are found to be biased low, and some data points are identified as outliers; these are excluded from further aerosol analyses in sections 4–8. The empirical histograms of PATMOS τ and α are found to be well-approximated with lognormal and normal probability density functions (PDFs), respectively (section 4). Retrievals of τ_2 are consistent with τ_1 at low τ , but are biased (multiplicatively) high, resulting in a low (additive) bias in α (section 5). A signal-to-noise ratio in α , defined by Ignatov and Stowe (2002b), is well approximated as $\eta = \tau_1/\tau_{10}$, but the parameter τ_{10} is found to be only $\sim 0.11 \pm 0.01$ in $\sim (110 \text{ km})^2$ PATMOS compared to $\tau_{10} \sim 0.18 \pm 0.02$ in $\sim (8 \text{ km})^2$ AEROBS data (section 6). This implies that the proportion of α retrievals with signal exceeding noise is higher in PATMOS relative to AEROBS because of the additional spatial averaging. Trends in aerosol retrievals are analyzed in section 7. Temporal artifacts are clearly traced in the data and are likely to be the result of residual calibration errors. Angular trends are fairly minor, and their nature seems to be well understood. However, PATMOS aerosols show a strong correlation with cloud amount, A_T , whose nature is not immediately clear. Trends with surface wind speed and integral water vapor are also observed. Note that these three latter analyses were not available from the AEROBS files. The PATMOS data differ from the AEROBS data by spatial resolution [$\sim (110 \text{ km})^2$ versus $\sim (8 \text{ km})^2$], cloud-screening algorithm, and sampling. The effect of those differences in the processing procedures as applied to the same input AVHRR GAC data in AEROBS is quantified in section 8 by mapping AEROBS data into PATMOS grid cells, and comparing the respective statistics of reflectances and aerosol retrievals. The differences are significant, especially in the Ångström exponent.

2. Aerosol retrievals

Aerosol retrievals are made with the independent-channel, 6S-RTM (Vermote et al. 1997) based algorithm documented in Ignatov and Stowe (2002a). AODs in AVHRR channels 1 and 2, τ_1 and τ_2 , are estimated by applying look-up-tables for each channel, LUT1 and LUT2, to the $(110 \text{ km})^2$ cloud-free mean reflectances in channels 1 and 2, ρ_1 and ρ_2 , and reported at the centroid wavelengths of $\lambda_1 = 0.63$ and $\lambda_2 = 0.83 \mu\text{m}$. The reflectance in channel i , ρ_i , is defined as

$$\rho_i = \frac{\pi L_i}{F_i \cos \theta_o}, \quad (1)$$

where $L_i (\text{W m}^{-2} \mu\text{m}^{-1} \text{sr}^{-1})$ and $F_i (\text{W m}^{-2} \mu\text{m}^{-1})$ are measured top-of-the-atmosphere (TOA) spectral radiance and solar flux, respectively, and θ_o is solar zenith angle. The TOA solar flux F_i changes with the Sun–

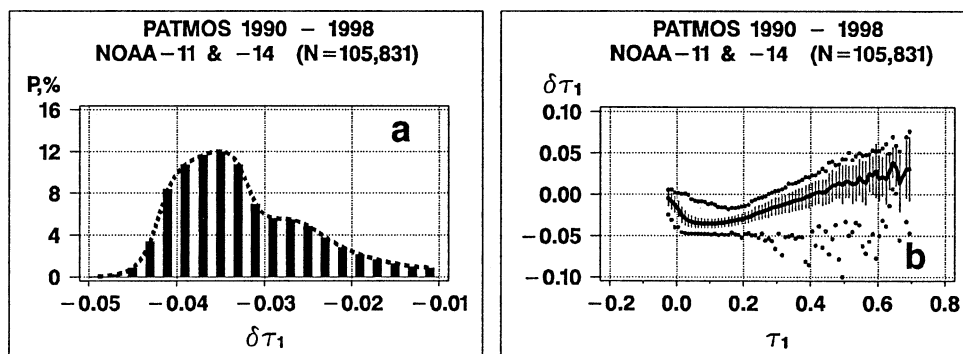


FIG. 2. Difference, $\delta\tau_1$, between τ_{1D} (Dave-based PATMOS estimate) and τ_1 (newly estimated using the 6S-based LUT1), $\delta\tau_1 \equiv \tau_{1D} - \tau_1$: (a) histogram of $\delta\tau_1$ (needles centered on $\Delta\delta\tau_1 = 2 \times 10^{-3}$ bins); (b) $\delta\tau_1$ as a function of τ_1 .

Earth distance d , as $F_i = F_{oi}/d^2$, where F_{oi} is the TOA flux normalized at $d = 1$. The values of F_{oi} for AVHRR channels on various NOAA satellites are summarized in Ignatov and Stowe (2002a). The PATMOS reflectances ρ_i , calculated with Eqs. (1)–(2), are thus conveniently normalized at the satellite- and channel-specific TOA solar fluxes, and normalized at Sun–Earth distance $d = 1$.

From τ_1 and τ_2 , an effective Ångström exponent is derived as

$$\alpha = \Lambda \ln\left(\frac{\tau_1}{\tau_2}\right), \quad \Lambda \equiv -\frac{1}{\ln\left(\frac{\lambda_1}{\lambda_2}\right)}. \quad (2)$$

For AVHRR channels 1 and 2 ($\lambda_1 = 0.63 \mu\text{m}$, $\lambda_2 = 0.83 \mu\text{m}$), the channels' spectral separation factor is $\Lambda \approx 3.63$. Physical principles and premises of this algorithm (termed internally at NOAA/NESDIS as the *second-generation* algorithm) have been analyzed in detail by Ignatov and Stowe (2000). Its technical implementation with the 6S RTM is documented in Ignatov and Stowe (2002a). In the original PATMOS distribution, only one AOD, τ_{1D} , was generated from ρ_1 with a Dave RTM-based LUT, which was set fixed for different satellites (Stowe et al. 2002). Retrieval of τ_{2D} was considered experimental at the time of production, and therefore it is not given in the dataset. The Phase I aerosol SST algorithm consequently uses two aerosol predictors: slant path AOD1, $x_1 = \tau_{1D} \times \sec\theta$ (here, θ is the satellite zenith angle), and clear-sky reflectance ratio, $x_2 = \rho_1/\rho_2$ (the latter being used as a proxy for aerosol particle size).

In this study, the τ_1 is re-derived, along with newly generated τ_2 and α , using 6S-based, satellite-specific LUT1 and LUT2 (Ignatov and Stowe 2002a). The NOAA-11 LUTs have been used for the first half of the 8-yr period (January 1990–December 1993) and the NOAA-14 LUTs for its second half (January 1995–December 1998).

Figure 2a plots a histogram of the differences between

the PATMOS Dave and 6S estimates of τ_1 , $\delta\tau_1 \equiv \tau_{1D} - \tau_1$, and Fig. 2b shows that $\delta\tau_1$ is τ -specific. The two prominent features of Fig. 2a are a negative bias in PATMOS τ_{1D} and a two-peak structure of the histogram of $\delta\tau_1$. The primary peak is found at $\delta\tau_1 \sim -3.5 \times 10^{-2}$, and the secondary peak is at $\delta\tau_1 \sim -2.5 \times 10^{-2}$. The Dave – 6S difference is much larger than $\delta\tau_1 < 1 \times 10^{-3}$ expected from the earlier analyses by Ignatov and Stowe (2002a), who compared Dave and 6S retrievals based on a *consistent* set of input parameters (Rayleigh, τ^R , and gaseous optical depths). However, the value of τ^R in the Dave LUT1 used for PATMOS processing (~ 0.0607 ; Stowe et al. 1997) is inconsistent with the new values for NOAA-11 and -14 (0.0569 and 0.0555, respectively; Table 2a in Ignatov and Stowe 2002a) found by accurate integration of their spectral responses with 6S. According to Ignatov and Stowe (2000), the (high) bias in the PATMOS τ^R , $\delta\tau^R \sim +0.0038$ and $+0.0052$ with respect to NOAA-11 and -14, should be scaled by a ratio of Rayleigh to aerosol phase functions (~ 6 – 7 , for average scattering geometry), to estimate the (low) bias in the retrieved τ_1 ($\delta\tau_1 \sim -0.025$ and -0.035 for NOAA-11 and -14, respectively).¹ This rough estimate based on single-scattering is in good quantitative agreement with the locations of the two peaks in Fig. 2a, which thus correspond to the two satellites. Their relative intensity is due to a lower number of NOAA-11 matchups in PATMOS–BUOY dataset. The number of global oceanographic buoy observations has steadily increased over 1990s, resulting

¹ The errors $\delta\tau^R \sim 5 \times 10^{-3}$ may seem too small to cause a significant $\delta\tau$ error. In sun photometry, $\delta\tau = -\delta\tau^R$, as τ is estimated by subtracting τ^R from the total optical depth. In satellite retrievals, aerosol path radiance ($\sim P\tau$) is estimated by subtracting Rayleigh path radiance ($\sim P^R\tau^R$) from the satellite signal. As a result, $\delta\tau \sim -(P^R/P) \times \delta\tau^R \sim -6 \times \delta\tau^R \sim 0.03$, which is $\sim 1/4$ of typical τ over oceans. The above $\delta\tau^R$ can be also compared to the natural fluctuations in τ^R . Typically, those are within $\sim \pm 1\%$ (Teillet 1990), but may reach $\sim \pm 4\%$. These *random* fluctuations in τ^R should be contrasted against the *systematic* differences between Dave and 6S of $\sim 8\%$ for AVHRR channel 1.

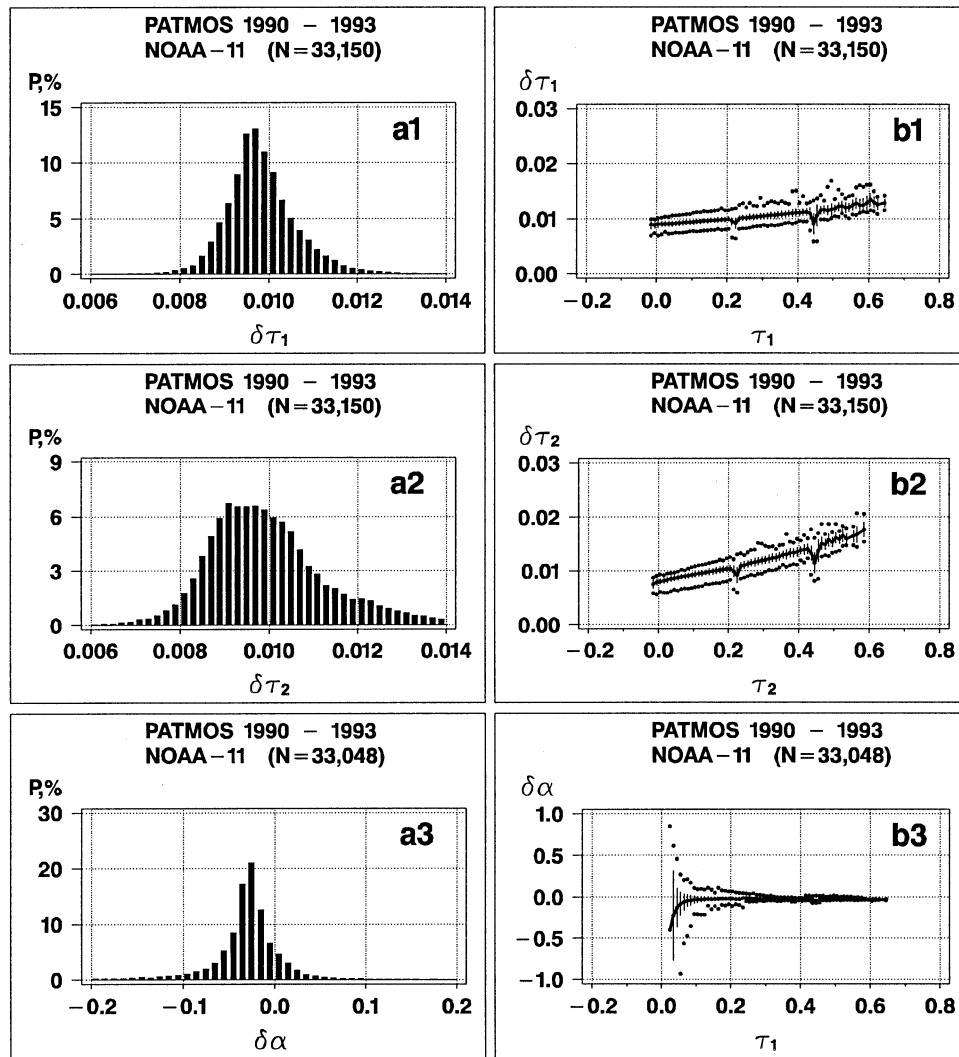


FIG. 3. Effect of using satellite-specific LUT in the retrievals from NOAA-11. Differences $\delta\tau_1$, $\delta\tau_2$, and $\delta\alpha$ are between respective retrievals made with NOAA-14 LUTs and NOAA-11 LUTs ("wrong minus correct"): (left) histograms of $\delta\tau_1$ and $\delta\tau_2$ (a1 – a2; needles centered on $\Delta\delta\tau = 2 \times 10^{-4}$ bins), and $\delta\alpha$ (a3; $\Delta\delta\alpha = 10^{-2}$); (right) $\delta\tau_1$ as a function of τ_1 (b1), $\delta\tau_2$ as a function of τ_2 (b2), and $\delta\alpha$ as a function of τ_1 (b3).

in a greater number of NOAA-14 matchups (Nalli and Stowe 2002).

To illustrate the importance of using satellite-specific LUTs, Fig. 3 quantifies the would-be error in τ and α , if NOAA-14 LUTs were used with NOAA-11 data. Negative differences in the respective τ^R (NOAA-14 minus NOAA-11), $\delta\tau_1^R \sim -0.0014$ and $\delta\tau_2^R \sim -0.0010$, result in positive τ errors of $\delta\tau_1 \sim \delta\tau_2 \sim +0.01$ (Figs. 3a1,a2). The errors in channels 1 and 2 are largely coherent (Figs. 3b1,b2), and partially cancel out in calculating the Ångström exponent, which is positively biased by only a few hundredths (Fig. 3a3). This bias depends upon τ , and becomes progressively more noticeable at $\tau < 0.1$ (Fig. 3b3).

It is therefore recommended that satellite-specific LUTs be used. The remainder of this paper is dedicated to the analyses of 6S-based retrievals, which have proved to be

more accurate and versatile than those made with the fixed Dave LUT (Ignatov and Stowe 2002a).

3. Quality control of retrievals

a. Retrievals at high solar zenith angles

Figure 4a shows the frequency distribution of solar zenith angle, θ_o , in the PATMOS-BUOY dataset, and Figs. 4b–d provide a statistical summary of the retrieved τ_1 , τ_2 (arithmetic mean, standard deviation, and minimum), and α (arithmetic mean and standard deviation), as a function of θ_o . The retrievals are fairly stable when $\theta_o < 60^\circ$, but develop progressively low biases at higher solar zenith angles with magnitudes of $\Delta\tau_1 \sim -0.07$ and $\Delta\tau_2 \sim -0.05$ (up to $\Delta\tau_1 \sim -0.20$ and $\Delta\tau_2 \sim -0.10$

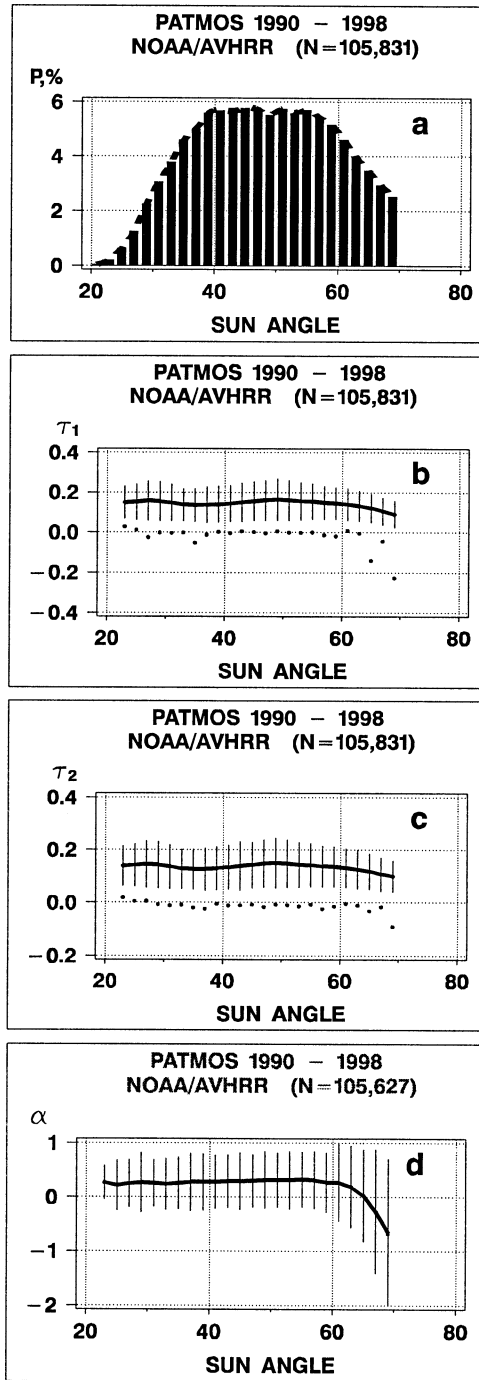


FIG. 4. (a) Histogram and effect of sun angle on retrievals of (b) τ_1 and (c) τ_2 and (d) α in the PATMOS-BUOY dataset. Sun angle is binned at $\Delta\theta_o = 2^\circ$ increment.

in extreme cases). The LUTs are known to cause negative errors in the retrieved τ (cf. Fig. 10 in Ignatov and Stowe 2002a), explaining about a half of the empirically observed effect. The unexplained portion of the bias suggests that other sources contribute to the overall error budget at slant angles, comparable in magnitude to the

TABLE 1. Number of observations used in plotting histograms in Figs. 1–2, and calculating statistics in Table 2.

QC test	Attribute	No. obs
<i>N</i> : Original data		87 246
$\tau_{1\min}/N(\tau_1 \leq 0)/\tau_{1\max}$ Original data		−0.05/16/1.46
$\tau_{2\min}/N(\tau_2 \leq 0)/\tau_{2\max}$ Original data		−0.02/65/2.01
1	$-\Delta N_{sp}$: Spectral test (section 3)	−77
2	$-\Delta N_{N1}$: ($\tau_1 \leq 0$)	−15
3	$-\Delta N_{N2}$: ($\tau_2 \leq 0$)	−53
4	$-\Delta N_{L1}$: ($\log \tau_1 > \log \tau_{g1} + 4 \log \mu_1$)	−2
5	$-\Delta N_{L2}$: ($\log \tau_2 > \log \tau_{g2} + 4 \log \mu_2$)	−1
6	$-\Delta N_{S1}$: ($\log \tau_1 > \log \tau_{g1} - 4 \log \mu_1$)	−49
7	$-\Delta N_{S2}$: ($\log \tau_2 > \log \tau_{g2} - 4 \log \mu_2$)	−133
	$-\Delta N$: Total excluded data (sum of previous seven lines)	−330 (0.38%)
<i>N</i> : Screened data		86 916
$\tau_{1\min}/\tau_{1\max}$: Screened data		0.01/1.21
$\tau_{2\min}/\tau_{2\max}$: Screened data		0.01/1.01

LUT-induced ones. Note that due to the reciprocity principle, similar errors are expected at zenith view angles $\theta > 60^\circ$. These angles, however, are not used in aerosol retrievals, due to the specifics of cloud masks in both PATMOS and AEROBS data. Figure 4d further suggests that errors in τ are incoherent in the channels, thus leading to a pronounced negative bias in the Ångström exponent of $\Delta\alpha \sim -1$ at $\theta_o > 60^\circ$. Until these biases at high sun zenith angles are better understood and corrected for, the use of this angle range is not recommended. Therefore, the $\Delta N_s = 18\,585$ observations with $\theta_o > 60^\circ$ ($\sim 17.6\%$ of data points) are removed from further analyses.

b. Outliers and other physically unrealistic retrievals

The remaining $N = 87\,246$ PATMOS retrievals have been further tested with a series of QC procedures described by Ignatov and Stowe (2002b). Results from these tests are listed in Table 1 (cf. with Table 1 in Ignatov and Stowe 2002b for AEROBS data) and described below.

Figure 5a shows a scattergram of τ_1 versus τ_2 , after removal of observations with high sun zenith angles but before QC. Some points fall well outside of the main cluster, due to radiometer malfunction, or significant departures in the ocean surface/atmosphere properties from those assumed in the retrieval model (e.g., a misclassified type of surface in PATMOS, or residual cloud in the sensor's field of view). Ignatov and Stowe (2002b) designed a special spectral statistical test (QC1) to remove the outliers. Applied to PATMOS data, this test identifies only $<0.1\%$ of data points ($\Delta N_{sp} = 77$), compared to typical $0.5\%–0.8\%$ in AEROBS data. This is because some otherwise “bad” GAC pixels might have migrated to the main body of the cluster within PATMOS, having been averaged together with many “good” GAC pixels within a $(110\text{ km})^2$ PATMOS grid cell.

The next two tests (QC2–3) check for a number of

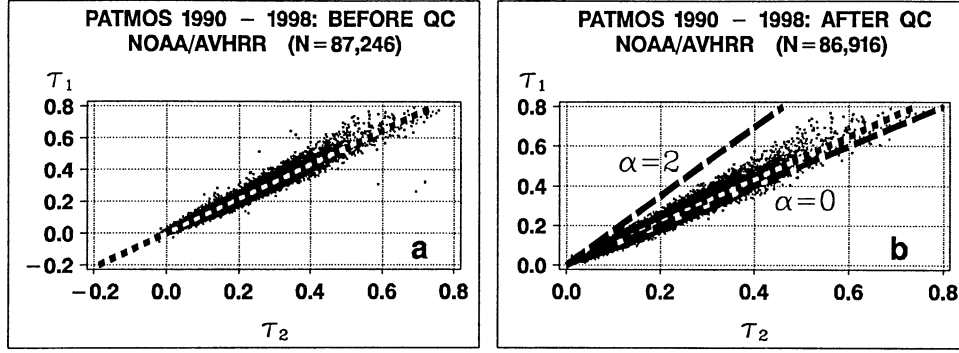


FIG. 5. Scattergram of τ_1 vs τ_2 (retrievals with $\theta_o > 60^\circ$ removed): (a) before QC tests described in Table 1; (b) after QC1–7. Short dashes show regression lines $\tau_1 = b + a\tau_2$. Long dashes correspond to $\alpha = 0$ and $\alpha = 2$.

negative retrievals in either channel. A total of $\Delta N_{N1} = 15$ data points with $\tau_1 < 0$, and $\Delta N_{N2} = 53$ additional data points with $\tau_2 < 0$ are found in the output of QC1 (note that the logic of the tests is cumulative, i.e., the test number $i + 1$ is applied to the result of test i). In contrast to QC1, these proportions are higher than those seen in AEROS data. This is probably due to residual calibration errors, which may become larger during certain periods within the 8-yr period under consideration. An empirical analysis by Ignatov (2002) suggests that calibration-induced errors in τ_1 and τ_2 are approximated as $\Delta\tau_1 \sim (0.37 + 0.71\tau_1)\varepsilon_1$, and $\Delta\tau_2 \sim (0.16 + 0.74\tau_2)\varepsilon_2$, where ε_1 and ε_2 are fractional calibration errors in the channels. For realistic calibration errors of $\varepsilon_1 \sim -0.05$ and $\varepsilon_2 \sim -0.07$, and $\tau_1 \sim \tau_2 \sim 0$ (it is the observations with smallest τ , which have the highest chance to cross over the $\tau = 0$ line), one obtains $\Delta\tau_1 \sim -0.02$ and $\Delta\tau_2 \sim -0.01$. Combining this with the effect of radiometric noise and digitization ($\sigma_{\tau_1} \sim 0.75 \times 10^{-2}$ and $\sigma_{\tau_2} \sim 1.0 \times 10^{-2}$ in pixel-level data; see Ignatov 2002), and probable significant anomalies in surface pressure (affecting τ^R ; see footnote 1) and surface reflectance, leads to negative errors comparable in magnitude with the minima in the original data listed in Table 1.

The last series of tests is based on identifying outliers, both high ($> \log\tau_{gi} + 4 \log\mu_i$; QC4–5) and low ($< \log\tau_{gi} - 4 \log\mu_i$; QC6–7), in $\log\tau$ space for channels 1 (QC4,6) and 2 (QC5,7), where the geometric mean τ_{gi} and standard deviation (STD) μ_i of τ_i in channel ($i = 1, 2$) are defined, respectively, as

$$\begin{aligned} \log\tau_{gi} &= \langle \log\tau_i \rangle; \\ \log\mu_i &= \sqrt{\langle (\log\tau_i - \log\tau_{gi})^2 \rangle}. \end{aligned} \quad (3)$$

The physical nature of the outliers is discussed by Ignatov and Stowe (2002b). The number of high outliers in PATMOS is fewer than in AEROS data (where it was from 5 to 50 points), most probably due to the fact that some GAC outliers have been averaged out with their less anomalous neighbors within a $(110 \text{ km})^2$ PATMOS grid cell. The number of low outliers is comparable in both data sources.

In total, the seven QC tests remove $\Delta N = 330$ observations. This is only 0.4% of data points, compared with 0.8%–1.3% in AEROS data. Although the $\sim 0.4\%$ – 1.0% reduction in outliers from AEROS to PATMOS might suggest improved data quality in PATMOS, it is probable that some PATMOS grid cells within the main body of points have been contaminated by the outlier GAC pixels resolved by AEROS. Figure 5b demonstrates the performance of the QC tests by replottting τ_1 versus τ_2 after removal of outliers. Note that all seven QC tests have been consistently used in all analyses below, except in section 7, where trends in the minima τ statistics are analyzed.

4. Probability density functions (PDFs) of τ and α

Ignatov and Stowe (2000) made an empirical observation that the shape of the τ histograms retrieved from the visible and infrared scanner (VIRS) on board the Tropical Rainfall Measuring Mission (TRMM) is close to lognormal. The α PDF was observed to be close to Gaussian, which is expected if the τ lognormality holds. O'Neill et al. (2000), and Kabanov and Sakerin (2000), provided further empirical evidence of τ lognormality based on the analyses of ground-based sun photometer measurements. Dubovik et al. (1995), and Dubovik and King (2000), suggest that there are fundamental theoretical considerations underlying the lognormality of the τ PDFs (Edie et al. 1971; Tarantola 1987). Ignatov and Stowe (2002b) tested these hypothesis with four large, yet space–time restricted, AVHRR (AEROS) datasets, and here we test them further using the global multiyear PATMOS–BUOY data.

a. PDF of aerosol optical depths

Figure 6 shows histograms of the quality-controlled τ_1 and τ_2 . Superimposed are their fits with lognormal PDFs (solid curves; O'Neill et al. 2000) (note that throughout this paper, we employ the shorthand notation, “log” and “ln” for referring to decimal, \log_{10} , and natural, \log_e , logarithms, respectively):

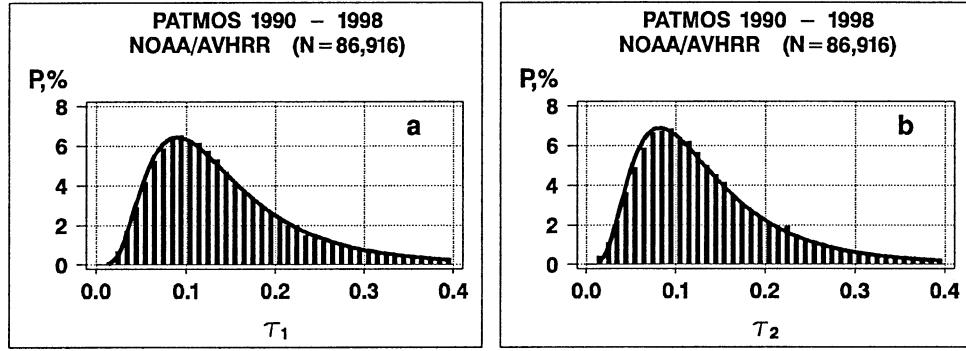


FIG. 6. Empirical histograms (needles centered on $\Delta\tau = 10^{-2}$ bins), and their fit with lognormal PDFs (solid line) of (a) τ_1 and (b) τ_2 . Data have been screened with QC1–7 tests described in Table 1.

$$P(\tau_i) = \frac{1}{\tau_i} \frac{1}{\ln 10} P(\log \tau_i);$$

$$P(\log \tau_i) = \frac{1}{\sqrt{2\pi} \log(\mu_i)} \exp \left[-\frac{\log^2 \left(\frac{\tau_i}{\mu_i} \right)}{2 \log^2(\mu_i)} \right]. \quad (4)$$

In evaluating the accuracy of the fit in Fig. 6, one should keep in mind that deviations from lognormality are expected empirically, due to residual instrumental and algorithm-related errors, even if AOD were theoretically distributed perfectly lognormal. One would also expect that the Mt. Pinatubo eruption in mid-1991 might introduce a distortion, and stand out as a separate peak (cluster) in the histograms. The histograms, however, remain monomodal and lognormally shaped, but with somewhat elevated parameters. This may be due to a relatively small proportion of NOAA-II observations in the PATMOS-BUOY dataset ($\sim 30\%$), only a fraction of which was corrupted by the Mt. Pinatubo eruption. Additionally, the stratospheric aerosol layer gradually diminished over a period of a few years.

Table 2 lists the *geometric* (τ_{gi} , μ_i) and *arithmetic*

(τ_{ai} , $\sigma\tau_i$) means and STDs in the retrieved τ . The two statistics differ by up to $\delta\tau \sim 0.02$ ($\sim 15\%$ of the typical τ signal). According to O'Neill et al. (2000), the use of geometric statistics is better justified than arithmetic (customarily used in the aerosol community), allowing for a more accurate reconstruction of the τ PDF. In addition to the 8-yr period, which includes the Mt. Pinatubo eruption, the two rightmost columns of Table 2 list Mt. Pinatubo-free statistics. The latter numbers provide a useful reference for a global marine background τ_1 and τ_2 (note, however, that the τ_2 statistics is most probably biased high as discussed in section 5).

b. PDFs of the Ångström exponent

Figure 7 shows histograms of the Ångström exponent α along with their fit using a normal PDF:

$$P(\alpha) = \frac{1}{\sqrt{2\pi}\sigma_\alpha} \exp \left[-\frac{(\alpha - \alpha_m)^2}{2\sigma_\alpha^2} \right], \quad (5)$$

where α_m and σ_α are ensemble arithmetic mean and standard deviation of the Ångström exponent. The shape

TABLE 2. Statistics of aerosol optical depths and Ångström exponents (after QC1–7).

	Full dataset (1990–93 and 1995–98; No. = 86 916)		Mt. Pinatubo excluded (1990 and 1995–98; No. = 67 662)	
	Mean	Std dev	Mean	Std dev
Aerosol optical depth in Ch1 (geometric statistics)	$\tau_{g1} = 0.126$	$\mu_1 = 1.787$	$\tau_{g1} = 0.113$	$\mu_1 = 1.712$
Aerosol optical depth in Ch2 (geometric statistics)	$\tau_{g2} = 0.117$	$\mu_2 = 1.802$	$\tau_{g2} = 0.106$	$\mu_2 = 1.736$
Aerosol optical depth in Ch1 (arithmetic statistics)	$\tau_{a1} = 0.149$	$\sigma\tau_1 = 0.093$	$\tau_{a1} = 0.130$	$\sigma\tau_1 = 0.077$
Aerosol optical depth in Ch2 (arithmetic statistics)	$\tau_{a2} = 0.138$	$\sigma\tau_2 = 0.085$	$\tau_{a2} = 0.123$	$\sigma\tau_2 = 0.072$
Ångström exponent				
Ångström exponent ($\tau_1, \tau_1 \geq 0.1$)	$\alpha_a = 0.28$	$\sigma_\alpha = 0.46$	$\alpha_a = 0.23$	$\sigma_\alpha = 0.47$
	$\alpha_a = 0.25$	$\sigma_\alpha = 0.34$	$\alpha_a = 0.22$	$\sigma_\alpha = 0.41$
	(No. = 52 479)	(No. = 52 479)	(No. = 39 107)	(No. = 39 107)

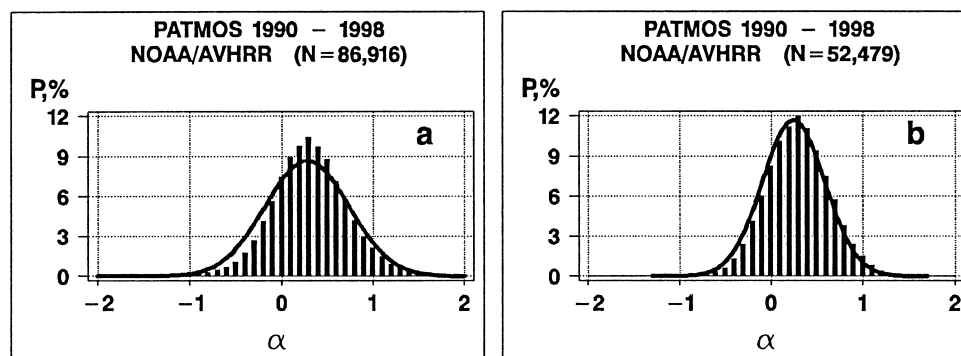


FIG. 7. Empirical histograms (needles centered on $\Delta\alpha = 1 \times 10^{-1}$ bins) and their fit with normal PDFs (solid line) of the Ångström exponent α , derived from τ_1 and τ_2 of AVHRR (screened with QC1-7 tests described in Table 1) using Eq. (1): (a) $\tau_1, \tau_2 \geq 0$, (b) $\tau_1, \tau_2 \geq 0.1$.

of the histograms in Fig. 7 is close to Gaussian, with deviations primarily due to retrieval error, which increases in inverse proportion to τ (see section 6 for details). To demonstrate this, Fig. 7b shows that histograms of α become closer to Gaussian, after excluding observations with $\tau_1, \tau_2 < 0.1$. The fit parameters, α_m and σ_α , for the two cases in Fig. 7 are listed in Table 2. The sample standard deviation of the Ångström exponent (σ_α) is more sensitive to the restrictions imposed on τ than the sample mean (α_m).

We thus conclude that PATMOS α is distributed normally, similar to the AEROS α . The empirical histogram may deviate from a normal shape, due to nonaerosol errors in the retrievals (deviations of actual retrieval conditions from those assumed in the retrieval model), or because of input data quality. The relative importance of these *additive* factors increase toward low τ .

5. Interconsistency of τ_1 and τ_2 : High multiplicative bias in τ_2

Returning to Fig. 5b, the retrievals are expected to fill in a two-dimensional sector, restricted by two straight lines corresponding to $\alpha = 0$ ($\tau_1 = 1.0\tau_2$) and $\alpha = 2$ ($\tau_1 \approx 1.736\tau_2$). These are shown with long dashes, the slopes of the lines, τ_1/τ_2 , being calculated from the respective Ångström exponents using Eq. (2). The least squares regression line is also shown with short dashes and described by equation $\tau_1 = -3 \times 10^{-4} + 1.0820\tau_2$. Three features are worth noting.

- 1) The scattergram converges at the origin. Failure to converge is plausible only when additive errors, inconsistent in the channels, are present. Since the best calibration available at the time (Rao and Chen 1999) was used in PATMOS processing, this coherence between the *independent* retrievals of τ_1 and τ_2 from two AVHRR channels indirectly confirms that the ocean reflectances used in the LUT1 and LUT2 are *interconsistent*.
- 2) The scattergram progressively diverges as τ increases, due to the natural variability in the Ångström

exponent. In the section 6, this observation forms the basis for a statistical procedure to estimate this variability from the data.

- 3) The cluster of retrievals is shifted from its expected domain. The Ångström exponent is generally known to be mostly positive. Its modal value typically ranges from 0.4 to 0.7 for maritime aerosols, but reaching up to ~ 1 when influenced by continental and other sources (e.g., Smirnov et al. 1995). In Fig. 5b, however, quite a few points are found below the $\alpha = 0$ line. The average Ångström exponent, estimated from the slope of the regression line, is $\alpha_o = \Lambda \ln(1.0820) \approx 0.29$. This regression-based estimate is consistent with the direct calculation of the ensemble mean listed in Table 2, but near the lowest boundary of its expected domain ($\alpha = 0$). If a more realistic global average value of $\alpha_o \sim 0.6$ – 0.8 (assuming continental influences) is adopted for the sake of estimate, then the slope of the regression line is expected to be from 1.18 to 1.25. Ignatov and Stowe (2002a,b) suggested that the observed (additive) bias in α of ~ -0.4 most probably results from a positive (multiplicative) bias in τ_2 that occurs from an overestimation of water vapor absorption contribution in 6S (recall that in 6S, all atmospheric absorption is placed above the scattering layer). Rough estimates suggest that τ_2 should be decreased by at least $\sim 12\%$, in order to bring α to its realistic range. This issue is currently being investigated quantitatively, and results will be reported elsewhere. Note that this systematic bias has no impact on the analyses of random errors in section 6 below.

6. Signal-to-noise ratio (SNR) in the Ångström exponent

If the PATMOS Ångström exponent is to be efficiently utilized in an aerosol correction algorithm for SST, its information content needs to be quantified. This analysis is also fundamental to future dependent-channel aerosol enhancements from AVHRR. This is because

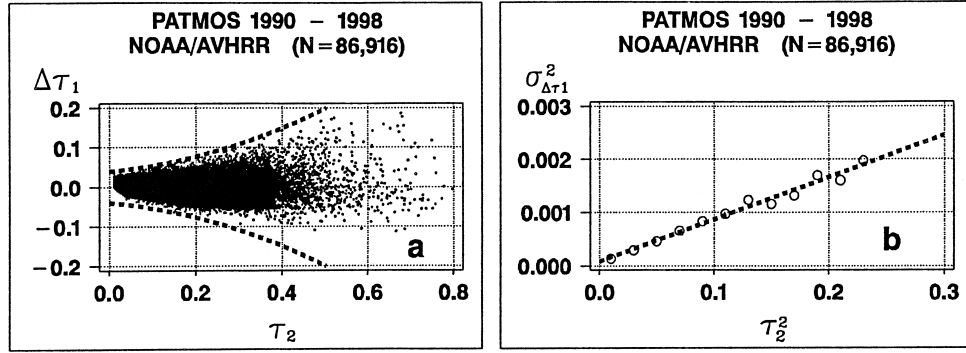


FIG. 8. (a) Regression (short dashes in Fig. 5b) residual, $\Delta\tau_1$, vs τ_2 with $\pm 4\sigma_{\Delta\tau_1}$ curves (dashed) superimposed; (b) mean square of the regression residual, $\sigma_{\Delta\tau_1}^2$ vs binned τ_2^2 (after QC1–7 in Table 1).

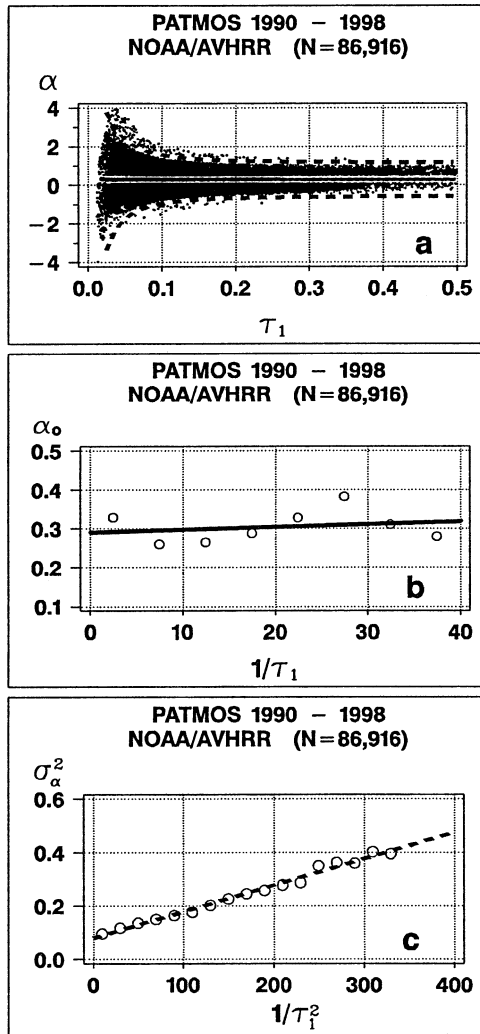


FIG. 9. (a) Scattergram of α vs τ_1 (after QC1–7 in Table 1) with mean, α_0 (solid) $\pm 3\sigma_\alpha$ (dashed) lines superimposed; (b) relationship of α_0 vs binned $1/\tau_1$ with linear fit superimposed; (c) relationship of σ_α^2 vs binned $1/\tau_1^2$ with linear fit superimposed.

any potential for improvement over the current independent-channel, fixed-aerosol-model approach is based upon the measured spectral information, quantitatively characterized by the Ångström exponent. Thus, the successful implementation of any simultaneous-solution algorithm critically depends upon the ability to measure this spectral information accurately. This section estimates the signal, noise and signal-to-noise ratio (SNR) in the PATMOS α , using procedures proposed by Ignatov and Stowe (2002b), and compares them with estimates from space and time restricted AEROS data.

a. Scattergrams of τ_1 versus τ_2

Figure 8a plots the residual of the regression shown in Fig. 5b, $\Delta\tau_1$, as a function of τ_2 . Ignatov and Stowe (2002b) suggest a linear relationship between $\sigma_{\Delta\tau_1}^2$ and τ_2^2 , with the slope, σ_a^2 , and intercept σ_b^2 of the regression being dependent on the natural (“noise free”) variance of the Ångström exponent within a dataset, $\sigma_{\alpha_0}^2$, and τ -retrieval *additive* errors (“noise”) in channels 1 and 2, σ_{1n}^2 and σ_{2n}^2 , as

$$\sigma_a^2 \approx \frac{\sigma_{\alpha_0}^2}{\Lambda^2}; \quad \sigma_b^2 \approx \sigma_{1n}^2 + \sigma_{2n}^2. \quad (6)$$

The empirical points, $\sigma_{\Delta\tau_1}^2$, estimated at binned values of τ_2^2 , are shown in Fig. 8b, along with a linear regression fit through them. The slope is $\sigma_a^2 \sim 80 \times 10^{-4}$, and the intercept is $\sigma_b^2 - (\sigma_{1n}^2 + \sigma_{2n}^2) \sim 0.8 \times 10^{-4}$. The natural variability in the Ångström exponent is estimated from σ_a^2 with Eq. (6) as $\sigma_{\alpha_0} \sim \sigma_a \Lambda \sim 0.32$.

b. Scattergrams of α versus τ

Figure 9a shows a scattergram of α versus τ_1 . The average trend in α (estimated from Fig. 9b) is denoted with the superimposed solid line, whereas the dotted lines denote $\pm 3\sigma$ (estimated from Fig. 9c). To better understand results of Fig. 9, recall that for an arbitrary point, the retrieved α is a superposition of a “physical” signal α_p and an error signal, α_e/τ (Ignatov et al. 1998; Ignatov and Stowe 2002b):

$$\alpha = \alpha_p + \frac{\alpha_e}{\tau}. \quad (7)$$

Stratifying the retrieved α by τ , and averaging Eq. (7) over ensemble of measurements gives

$$\alpha_o(\tau) = \alpha_{op} + \frac{\alpha_{oe}}{\tau}. \quad (8)$$

Figure 9b suggests no noticeable $1/\tau$ -type *trend* in the average Ångström exponent, which, if available, would be indicative of a *systematic* error in α [i.e., if $\alpha_{oe} \neq 0$ in Eq. (8)].

The respective τ -stratified STD is

$$\sigma_\alpha^2(\tau) = \sigma_{ao}^2 + \frac{\sigma_{ae}^2}{\tau^2}. \quad (9)$$

Equation (9) suggests that the variance in the retrieved Ångström exponent, σ_α^2 , is proportional to $1/\tau^2$. The respective correlation between these two variables is shown in Fig. 9c. The intercept is $\sigma_{ao}^2 \sim 0.08$, from which $\sigma_{ao} \sim 0.28$. Comparing this number with the $\sigma_{ao} \sim 0.32$, estimated in section 6a from the “ τ_1 – τ_2 ” scattergram, one arrives at an average estimate of $\sigma_{ao} \sim 0.30 \pm 0.02$. The slope is $\sigma_{ae}^2 \sim 10^{-3}$, from which $\sigma_{ae} \sim 3.2 \times 10^{-2}$. A random error in the Ångström exponent can be alternatively estimated using the results of τ_1 – τ_2 analyses in section 6.1 as $(\sigma_{ae}^2/\tau^2) \equiv (\Lambda/\tau_1)^2 \times (\sigma_{n1}^2 + \sigma_{n2}^2)$ (Ignatov and Stowe 2002b). Substituting $(\sigma_{n1}^2 + \sigma_{n2}^2)^{1/2} \sim 0.89 \times 10^{-2}$, one obtains $\sigma_{ae} \sim \Lambda(\sigma_{n1}^2 + \sigma_{n2}^2)^{1/2} \sim 3.63 \times 0.89 \times 10^{-2} \sim 3.2 \times 10^{-2}$, in agreement with the above “ α – τ ” diagram based estimate.

c. Signal-to-noise ratio in PATMOS α

The estimates of “physical signal” and “noise” in the Ångström exponent allow one to define the SNR from Eq. (9) as $\eta = (\sigma_{ao}/\sigma_{ae})\tau_1 \equiv \tau_1/\tau_{10}$. The SNR increases linearly with τ_1 , and reaches a “cross-over” point in τ_1 , τ_{10} , where $\eta = 1$: $\tau_{10} \sim (\sigma_{ae}/\sigma_{ao}) \sim 0.032/(0.30 \pm 0.02) \sim (0.11 \pm 0.01)$. As τ_1 increases from τ_{10} , the measured α is progressively less impacted by “noise.” Sources of noise include radiometric error, along with errors introduced from departure of the prescribed nonaerosol model parameters from the observational conditions. Note that the Phase I SST tropospheric aerosol correction is only applied to data with observed $\tau_1 > 0.15$ (Nalli and Stowe 2002).

d. PATMOS versus AEROS signal-to-noise ratio

It is interesting to compare the above PATMOS estimates with those derived previously from AEROS data in Ignatov and Stowe (2002b): $\sigma_{ao} \sim 0.24 \pm 0.02$, $(\sigma_{1n}^2 + \sigma_{2n}^2) \sim 1.0 \times 10^{-4}$, $\sigma_{ae} \sim (4.2 \pm 0.2) \times 10^{-2}$, $\tau_{10} \sim 0.18 \pm 0.02$. The noise is reduced in the $(110 \text{ km})^2$ PATMOS τ and α , compared to the $(8 \text{ km})^2$ AEROS data, due to the additional spatial averaging. This reduc-

tion, however, is not proportionate to the increased area (sample size), as would be expected in the case of fully noncorrelated errors in retrievals (e.g., resulting from radiometric noise and digitization). This may indicate that the *spectrally incoherent* τ errors, causing random errors in α , mostly come from the physical factors in the retrieval model (residual cloud in a GAC field of view, surface reflectance and pressure, water vapor in channel 2) which are *spatially coherent* on the scales comparable to the PATMOS grid cell size. The included GAC outliers within PATMOS grid cell, which would allow screening out in AEROS (cf. section 3b), may also diminish the noise reduction in the PATMOS aerosol retrievals from what is otherwise expected.

As expected, the natural variability (“signal”) in the global 8-yr data PATMOS–BUOY Ångström exponent ($\sim \pm 3\sigma_{ao} \sim \pm 0.90$, in good agreement with a commonly used estimate of the range of this parameter $\sim \pm 1$; e.g., Smirnov et al. 1995) is larger than in the space–time restricted AEROS data analyzed in Ignatov and Stowe (2002b) ($\sim \pm 3\sigma_{ao} \sim \pm 0.72$).

7. Aerosol parameter trends

Aerosol retrievals are expected to reveal natural variations as a function of space and time, but should not contain artificial trends in time, sun-view–scattering–reflection geometry, or ambient cloudiness (Ignatov and Stowe 2000). An important prerequisite for using some of the statistical techniques of this section is uniform coverage of the respective space–time angle bins. This requirement is better satisfied in the PATMOS dataset due to its global, long-term nature than in the space–time restricted AEROS datasets used by Ignatov and Stowe (2002b).² Note that for the analyses of this section, QC4–5 were lifted (negative τ in both channels allowed), for the analyses of trends in τ_{\min} .

a. Temporal

Figure 10 shows time series of aerosol retrievals, along with the respective sample size. The left (NOAA-11) and central (NOAA-14) sets of panels are constructed on monthly basis. The right panel summarizes the two on a yearly basis, to underscore the long-term multiyear trends/discontinuities in the data. Three statistics are

² Analyses of this section will be shown to identify artificial trends in some parameters, against which aerosol retrievals are tested. Strictly speaking, not all these parameters are fully independent, and they may reveal false intercorrelations. For instance, certain scattering geometries are preferentially observed at certain latitudes, due to the NOAA orbital configuration. As a result, the actual causes for some biases are not easy to properly attribute. One may be tempted to exclude from all further analyses the domains of a parameter identified as troublesome at a certain stage of analysis. However, this section is meant to provide a *preliminary* assessment of the PATMOS product on a consistent basis, leaving more in-depth diagnostics and fixes for future research.

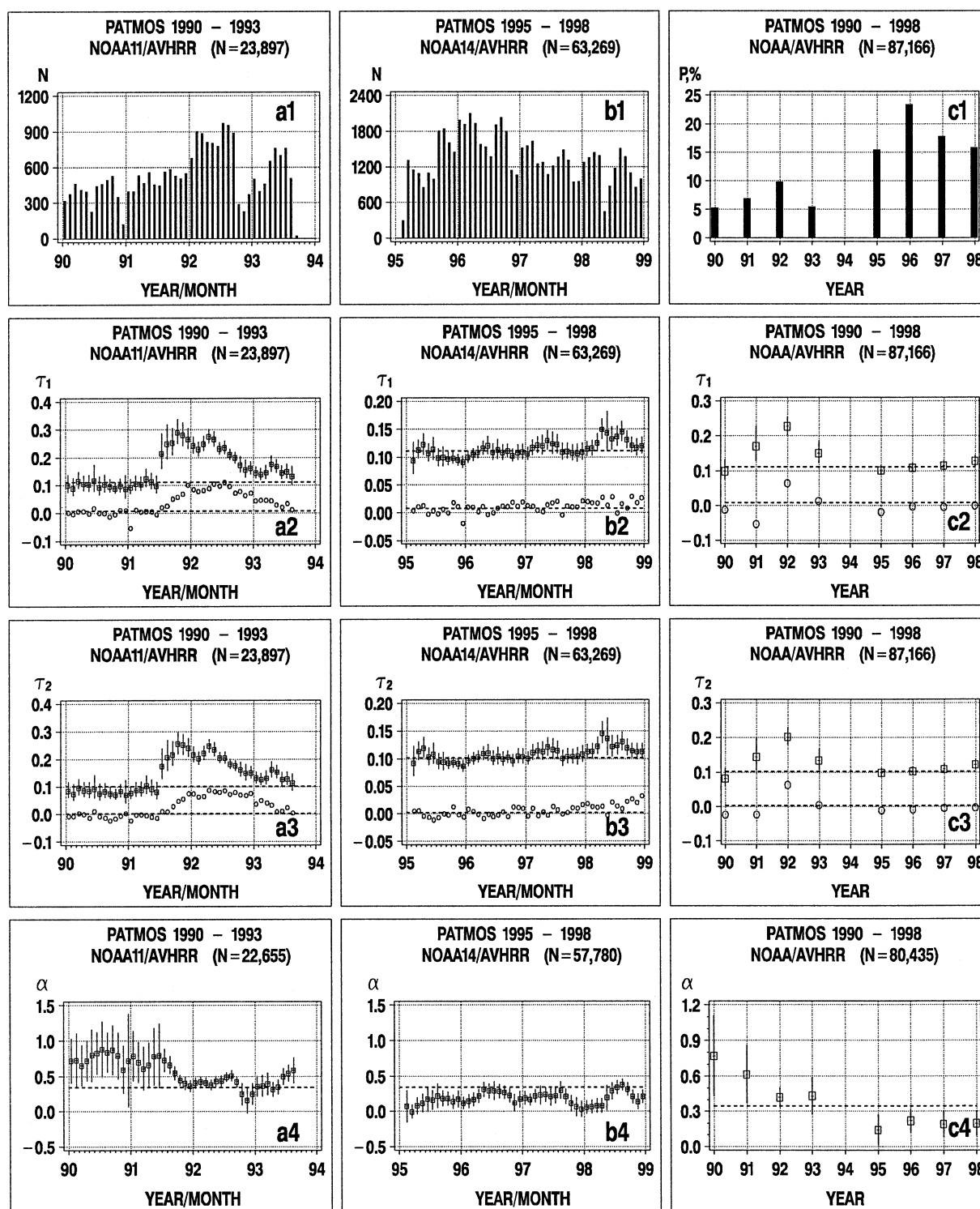


FIG. 10. Monthly statistics of number of observations, and aerosol retrievals for NOAA-11 (left column), NOAA-14 (center column), and yearly statistics for both satellites (right column): minimum (circle; for τ_1 and τ_2 only), mean (box), and $9 \times \sigma/\sqrt{N}$ (whisker; in yearly statistics, $30 \times \sigma/\sqrt{N}$). Note that whiskers are at $9 \times \sigma/\sqrt{N}$ in Figs. 11–16. The scaling factors chosen for illustration purposes only. For discussion on the standard error of mean see Ignatov and Stowe (2002b), section 5a. Horizontal dashed lines are at the mean level of each variable. Note that the τ statistics are calculated geometrically, and the α statistics are calculated arithmetically for $\tau_1, \tau_2 \geq 0$ (Ignatov and Stowe 2002b).

shown: mean, standard error (shown exaggerated), and minimum. The results emerging from Fig. 10 are discussed below.

The number of observations from *NOAA-14* is, on average, 3 times larger than from *NOAA-11*, due to a dramatically increased density of buoy observations in the late 1990s (viz., the inception of the TOGA-TAO array along with increasing numbers of drifting buoys). The last three months of *NOAA-11* (October–December 1994) are missing due to high solar zenith angle ($\theta_o > 60^\circ$).

NOAA-11 τ records were strongly disturbed by the dramatic eruption of Mt. Pinatubo in June 1991. A spike in observed τ (September 1991) is seen to exceed the background τ both in the mean (by about 3 times in the two AVHRR channels) and minimum τ statistics. In 1993, τ diminished to near pre-eruption levels, but still remained elevated by a few hundredths of τ unit, due to either continued post-eruption relaxation or residual calibration error. The *NOAA-14* τ records in both channels are more stable, but show increasing trends, in both mean and minimum, amounting to a few hundredth of τ unit toward the end of the satellite lifetime over a period of four years. These trends are more clearly traced in the yearly, rather than monthly, statistics, in the right column of Fig. 10. Estimates in section 3b suggest that the magnitude of the trends in *NOAA-14* could be well explained by residual calibration error of $(-5\% - 7\%) (4 \text{ yr})^{-1}$. The coherent character of the trends in channels 1 and 2 may result from a consistent vicarious calibration technique by Rao and Chen (1999) used for both channels. These observations support Ignatov's (2002) suggestion that the observed artificial trends in AVHRR τ time series can be used to adjust for residual calibration errors.

The trends in α are not as easy to interpret as in τ . A coherent part of the artificial trends in τ_1 and τ_2 essentially cancels out while taking their ratio in calculating the Ångström exponent. However, the remaining incoherent errors in τ_1 and τ_2 lead to substantial artificial trends in α , especially at low τ , due to a high sensitivity of the Ångström exponent to different nonaerosol-related modeling errors, as discussed in section 6. Ignatov (2002) suggested that this high α sensitivity may be used to detect the *incoherent* errors in τ_1 and τ_2 . Correcting for these errors is not straightforward, however, as one has to decide which channel should be trusted better. Figure 10 suggests that artificial trends in the *NOAA-11* α may reach 0.4–0.6 units of α (whose natural range of variability is ~ 2), masking even the Mt. Pinatubo signal. These trends may need to be corrected before the α data for *NOAA-11* are useable for SST correction, but these adjustments are beyond the scope of this study. Note that these errors in α did not critically corrupt our previous analyses (in particular, in section 6), due to a relatively small proportion of *NOAA-11* data in the PATMOS-BUOY dataset ($\sim 25\%$).

b. Geographical

Figure 11 shows the same statistics as above as a function of latitude, φ (left) and longitude, λ (right column). The geographical distribution of the retrieved parameters is realistic. In particular, higher τ and α in the Northern Hemisphere may indicate larger contamination by smaller continental particles. Spikes in the τ and α versus longitude occur coherently in the areas near the major crossings of the continent/ocean boundaries. Interpretation of some other features may be not as straightforward, however. For instance, elevated τ_1 and τ_2 are observed in the zonal belt associated with the intertropical convergence zone (ITCZ) between 5° and 15°N , and at high latitudes. Cloud amount derived from PATMOS data suggest that these areas are generally more cloudy. The correlation between aerosol τ and cloud amount is examined in section 8. The belt around $\sim 30^\circ\text{S}$ in latitude, and areas associated with the Indian and Pacific Oceans in longitude, appear to be the cleanest over the entire globe.

c. Angular

Figures 12 and 13 show sun-view-scattering-glint angle trends in aerosol retrievals. The lack of trends in the minima τ indicates a high degree of interconsistency between the instrumental calibration in PATMOS data, on the one hand, and treatment of nonaerosol physical factors (Rayleigh optical depths and ocean surface reflectance) in the 6S-RTM based retrieval model, on the other. Recall that in the space-time restricted AEROS data, both $\tau_{1\text{min}}$ and $\tau_{2\text{min}}$ showed an increasing trend by $\Delta\tau \sim 0.01\text{--}0.02$ over the full range of any of the four angles.

Artificial angular trends in the mean τ are traced in the view (Fig. 12), and scattering and glint angles (Fig. 13). Elevated τ at scattering angle $\chi > 160^\circ$, and at glint angle $\gamma < 50^\circ$, also have been observed in AEROS data, but the view angle trends are now stronger than seen before. Increased τ at a low glint angle most probably comes from increased specular reflection around the glint area (current retrievals are restricted to outside the 40° cone angle around the specular reflection point) at surface wind speeds higher than $V = 1 \text{ m s}^{-1}$ as currently assumed in the retrievals.³ The scatter angle trend may be caused by a

³ Wind speed was set to a constant of $V = 1 \text{ m s}^{-1}$ to avoid the necessity of setting the wind direction in the 6S *anisotropic* formulation (see discussion in Ignatov and Stowe 2002a). Customarily, the surface roughness is characterized using an *isotropic* Cox–Munk distribution of surface slopes (e.g., Tanre et al. 1997; Wagener et al. 1997; Mishchenko et al. 1999; Higurashi and Nakajima 1999). We know of no analyses which would compare the two formulations for the purpose of establishing the adequate one for the use in aerosol remote sensing. Furthermore, in the vast majority of current aerosol retrieval algorithms a constant surface wind speed is assumed [a case study by Wagener et al. (1997) being the rare exception]. For example, Tanre et al. (1997), Mishchenko et al. (1999), and Higurashi and Nakajima (1999) have assumed $V = 7 \text{ m s}^{-1}$, which is close to the median wind speed observed in the PATMOS-BUOY dataset ($V = 5\text{--}6 \text{ m s}^{-1}$, see Fig. 20a).

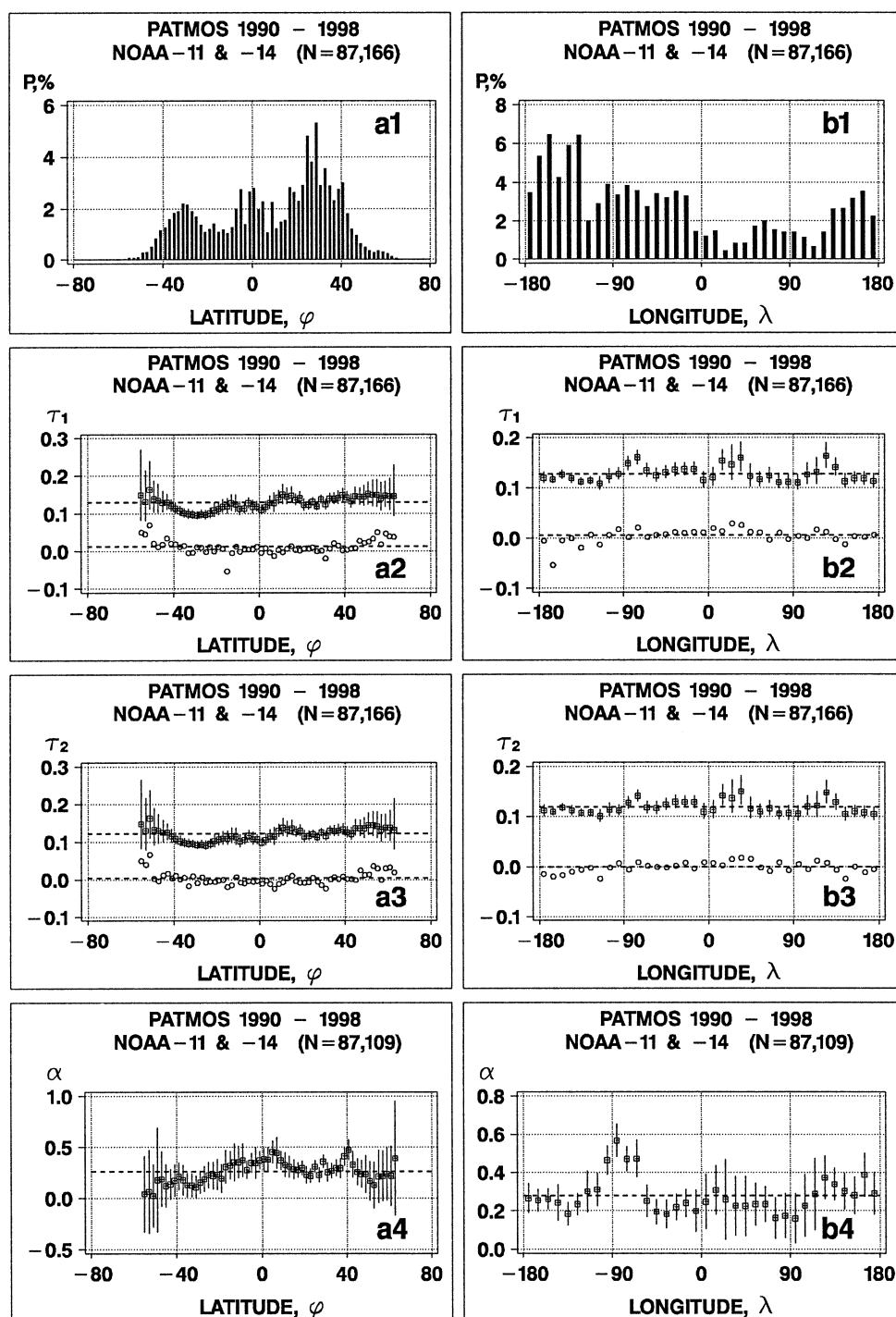


FIG. 11. Same as in Fig. 10 but (left column) vs latitude, φ (negative in Southern Hemisphere, $\Delta\varphi = 2^\circ$) and (right column) longitude, λ (negative in Western Hemisphere, $\Delta\lambda = 10^\circ$).

deviation of the model aerosol phase function from the actual phase function average over the oceans in back-scatter. Alternatively, it may result from the regional biases in the scatter geometry due to the specific NOAA orbital configuration, which may also explain the view angle and high glint angle ($\gamma > 100^\circ$) trends.

The Ångström exponent amplifies small uncertainties in τ through multiplication by the coefficient $\Lambda = 3.63$ in Eq. (2). As a result, the angular trends in α are more notable than in τ , and may offer a more subtle tool for identifying otherwise undetectable trends in τ .

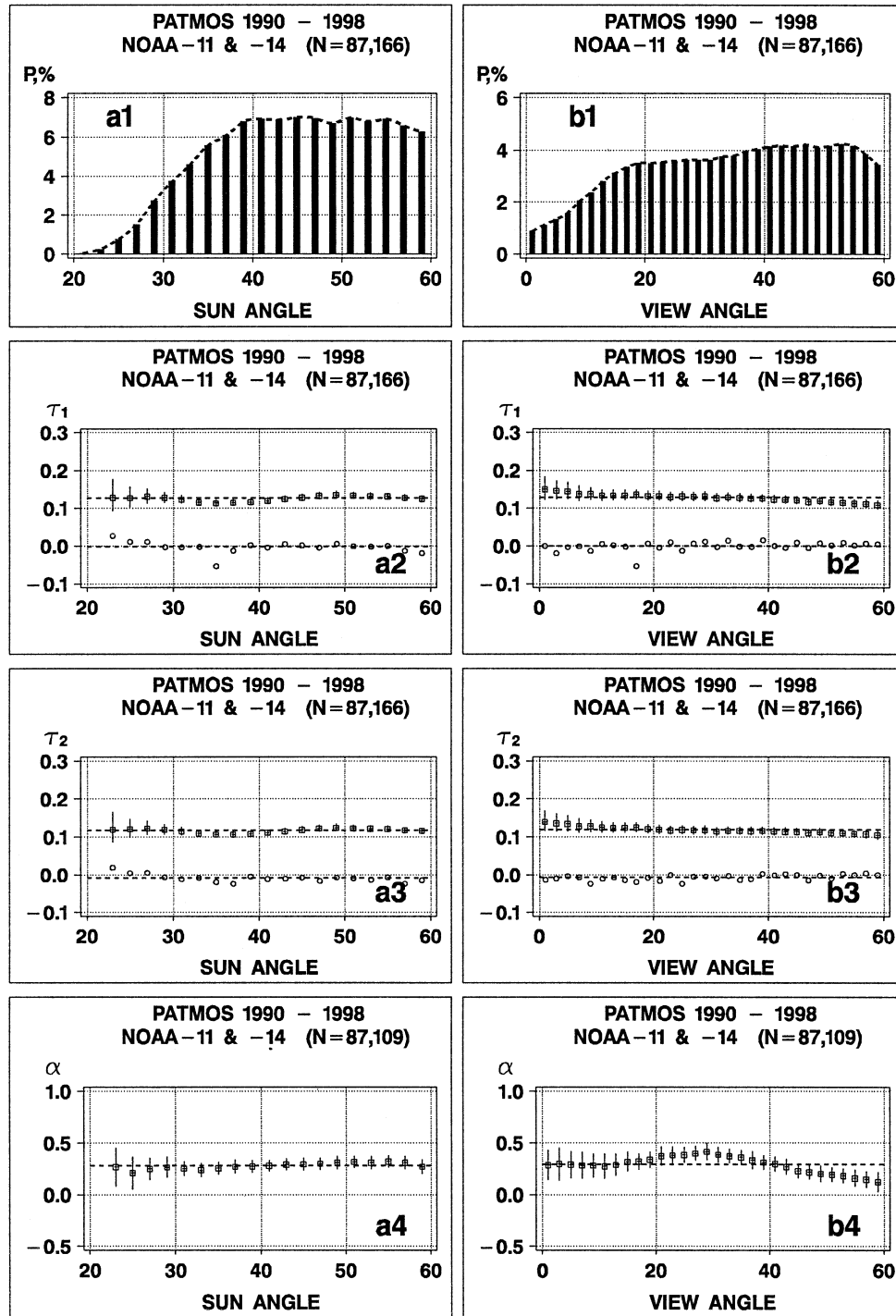


FIG. 12. Same as in Fig. 10 but (left column) vs sun angle, θ ($\Delta\theta_s = 2^\circ$) and (right column) view angle, θ_v ($\Delta\theta_v = 2^\circ$).

d. Cloud amount

Each PATMOS $(110 \text{ km})^2$ grid cell contains a number of clear and cloudy pixels, and a total cloud amount, A_T , estimated using a statistically equivalent spatial coherence (SESC) technique (Stowe et al. 1999). The left

column of Fig. 14 plots a histogram of A_T , and aerosol retrievals as a function of A_T . Note that the A_T is a *conditional* estimate: Only those PATMOS cells that have at least one pixel suitable for aerosol retrieval were used. There are strong trends in all aerosol parameters

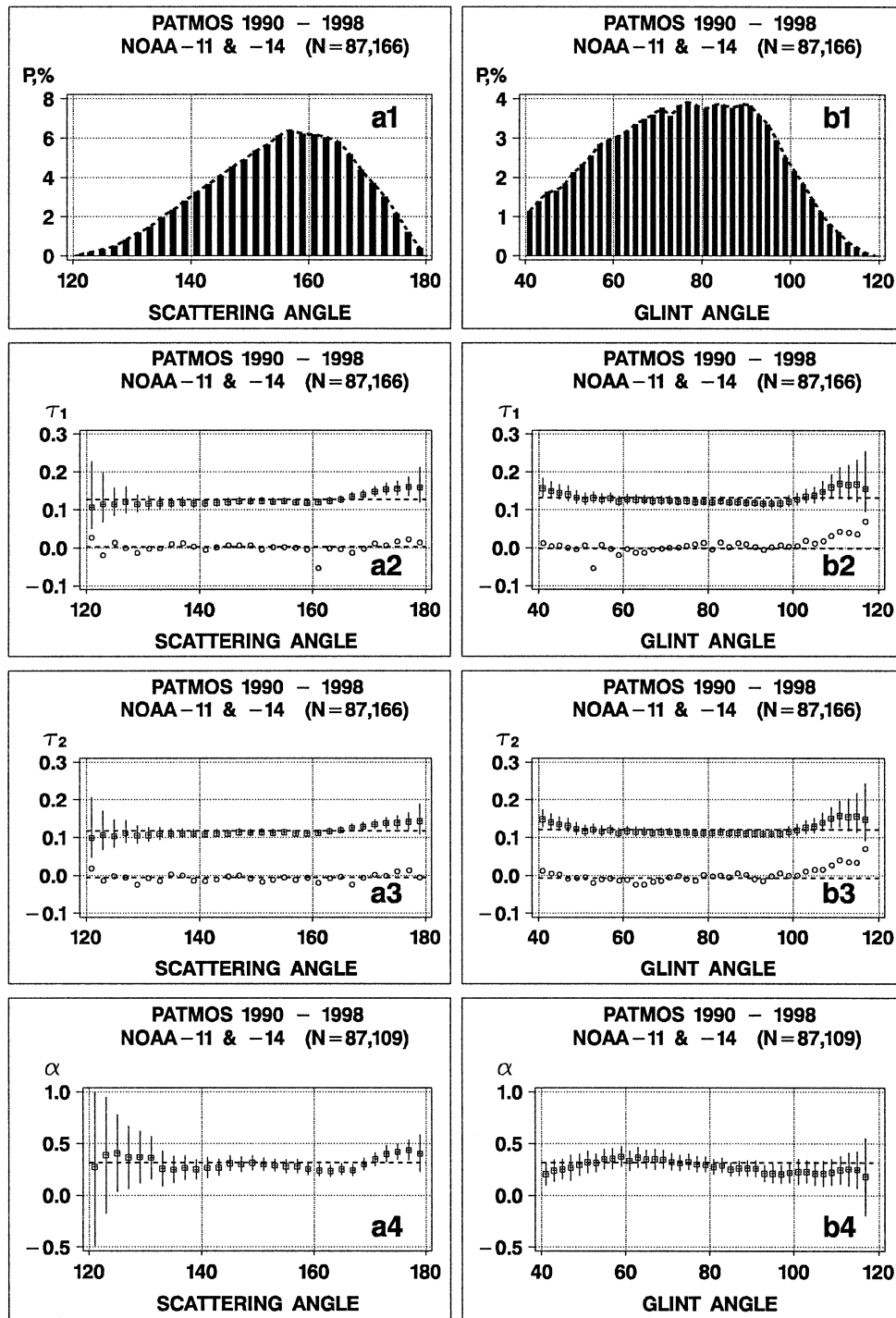


FIG. 13. Same as in Fig. 10 but (left column) vs. scattering angle, χ ($\Delta\chi = 2^\circ$) and (right column) glint angle, γ ($\Delta\gamma = 2^\circ$).

against A_T , and similar trends have been recently observed in TRMM VIRS aerosol retrievals (Ignatov et al. 2002). These could be attributed to the indirect aerosol forcing, resulting from increased hygroscopic aerosol particles that favorably influence cloud formation. Or, alternatively, aerosol retrievals could be affected by

residual cloud in the cloud-free portion of a $(110 \text{ km})^2$ grid cell. The probability of this latter effect apparently increases with increasing total ambient cloudiness, measured by the A_T parameter. Note that trends in τ_{\min} may suggest the retrieval artifact, as the intensity of cloud-aerosol interaction is expected to diminish in proportion

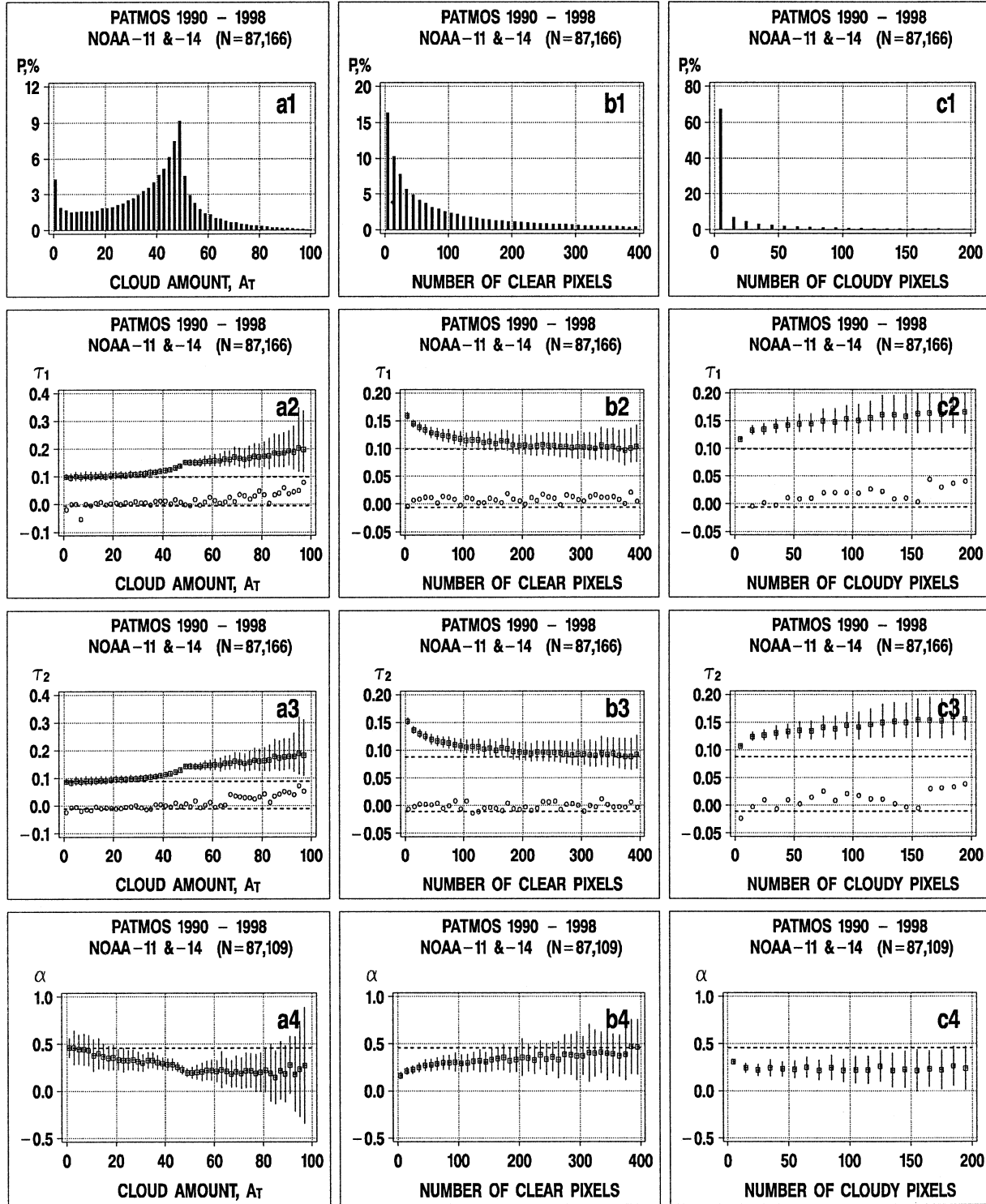


FIG. 14. Same as in Fig. 10 but (left column) vs cloud amount, A_T ($\Delta A_T = 2\%$) (center column) number of clear pixels ($\Delta N_{CLR} = 10$), and (right column) number of cloudy pixels ($\Delta N_{CLD} = 10$). Horizontal dashed lines are at the mean level of each variable calculated for $A_T < 5\%$ only.

to τ , due to decreased concentration of cloud condensation nuclei (CCN). On the other hand, the cases with high τ may be screened out by the cloud screening algorithm, which may result in low bias in τ .

The center and right columns of Fig. 14 show similar analyses with respect to the number of clear and cloudy pixels within a PATMOS cell. Trends similar to the A_T trend (and apparently related to it) are also observed. It is not immediately clear how to attribute the observation in Fig. 14. Since there is a plausible physical explanation, we have retained all data in the current analyses. However, the ambiguity needs resolving through further investigation.

e. Surface wind speed

In the merged, quality-controlled PATMOS-BUOY subset ($N = 87\,246$), mean surface wind speed, V (m s^{-1}) is available only for $N = 12\,266$ data points as it is measured only by some (viz., moored) buoys. Figure 15 plots the V trends in aerosol retrievals. Both mean and minimum τ increase by $\delta\tau_1 \sim +0.05$ and $\delta\tau_2 \sim +0.06$, when wind speed increases from 0 to 12–13 m s^{-1} . Despite the high degree of coherence in $\delta\tau_1$ and $\delta\tau_2$, the Ångström exponent declines by a $\delta\alpha \sim -0.5$. Similar trends, and of a comparable order of magnitude, have been previously observed in the τ and α measured by ground-based sun photometers (Platt and Patterson 1986; Smirnov et al. 1995; Kabanov and Sakerin 2000; Wilson and Forgan 2002). A retrieval artifact is also possible due to the incomplete treatment of the surface reflectance in the retrievals. The Lambertian (diffuse) surface reflectance is customarily set to zero (e.g., Tanre et al. 1997; Mishchenko et al. 1999; Higurashi and Nakajima 1999). Ignatov and Stowe (2002a) used $\rho_1^s = 2 \times 10^{-3}$ and $\rho_2^s = 5 \times 10^{-4}$, respectively, which approximately correspond to $V \approx 5$ – 7 m s^{-1} . Higher winds sharply intensify the formation of bright foam (white caps) on the surface, thus increasing the TOA reflectance (e.g., Wagener et al. 1997). The retrieval algorithm may incorrectly interpret this elevated reflectance as a higher aerosol signal. Figure 13b further suggests that using a constant wind speed of $V = 1 \text{ m s}^{-1}$ leads to artificially elevated τ at $\gamma < 50^\circ$ (Fig. 13b). Its magnitude ($\delta\tau_1, \delta\tau_2 \sim +0.03$ – $+0.05$), and the proportion of contaminated data ($<10\%$), however, may explain only a small part of the effect observed in Fig. 15.

f. Column water vapor

The integral (column) water vapor W (g cm^{-2}) is also available on the merged PATMOS-BUOY for a subset of matchups ($N = 60\,928$). Figure 16 plots aerosol statistics as a function of W . Trends are small in both τ_1 and τ_2 , but τ_2 seem to slightly decline with W . Analyses from ground-based sun photometers suggest an increasing trend against the surface relative humidity (RH) (e.g., Smirnov et al. 1995; Kabanov and Sakerin 2000).

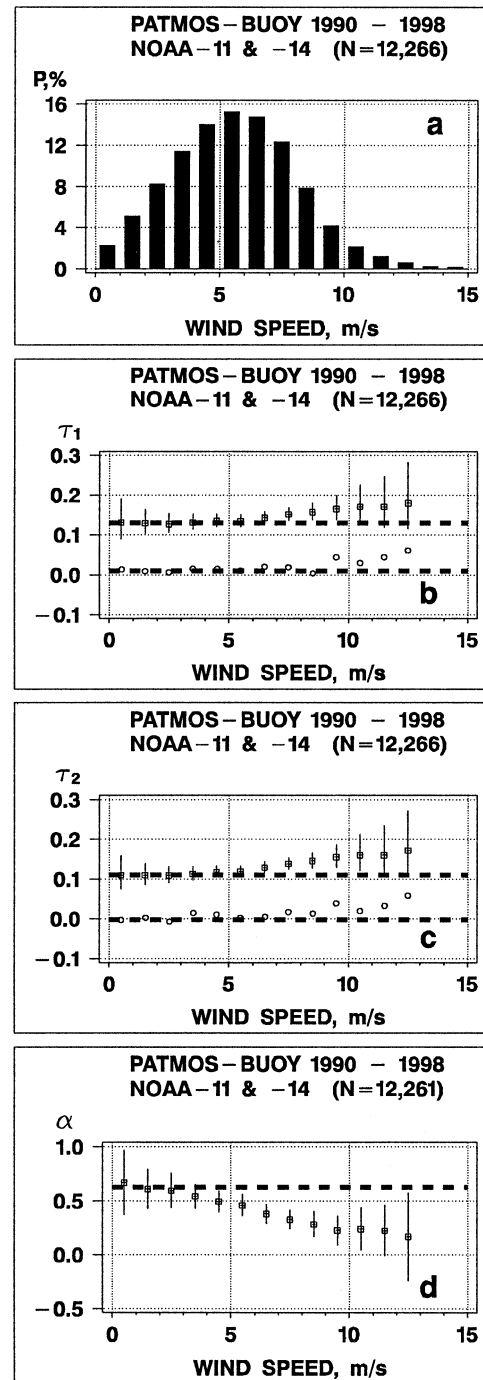


FIG. 15. Same as in Fig. 10 but vs mean surface wind speed (binned at $\Delta V = 1 \text{ m s}^{-1}$). Horizontal dashed lines are at the mean level of each variable calculated for wind speed $< 3 \text{ m s}^{-1}$ only.

Direct comparison of the W and RH results is not straightforward. Note, however, that an *artificial* water vapor trend in AVHRR channel 2 is expected, as this channel is strongly contaminated by variable water vapor absorption (recall that the current algorithm assumes a constant water vapor profile based on the midlatitude

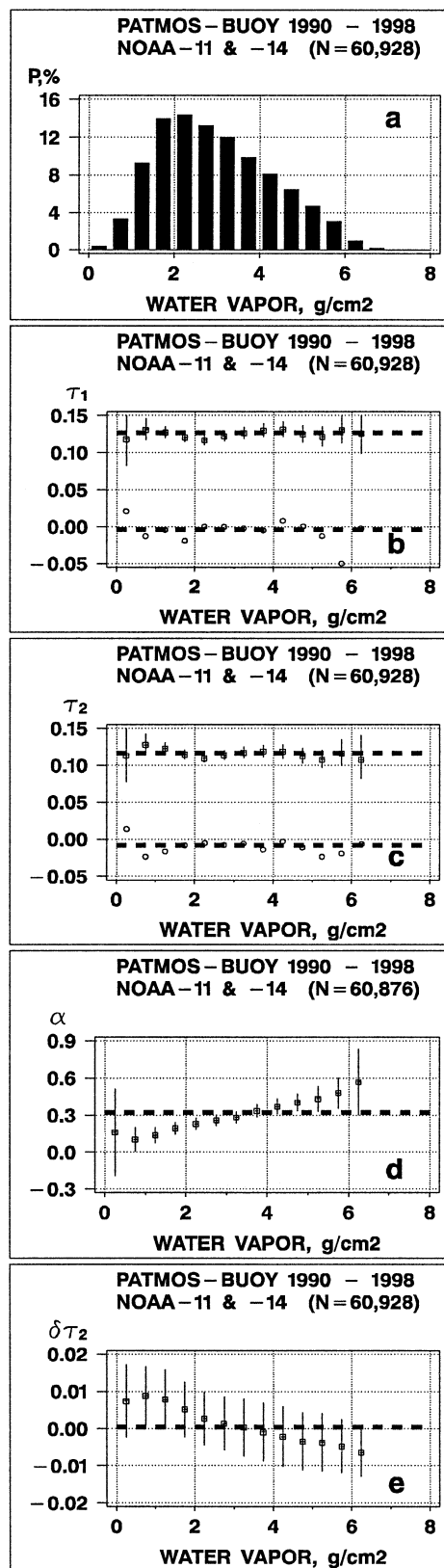


FIG. 16. Same as in Fig. 10 but vs total column water vapor (binned at $\Delta W = 0.5 \text{ g cm}^{-2}$). Horizontal dashed lines are at the mean level of each variable calculated for the whole range of water vapor. Note that in (e), vertical bars are half-standard deviations.

summer standard atmosphere; Ignatov and Stowe 2002a). Figure 16e plots a regression residual of τ_2 versus τ_1 , $\delta\tau_2 = \tau_2 - (a + b\tau_1)$, the term in parentheses being a least squares predictor of τ_2 from τ_1 . This differencing is meant to remove the physical dependence of $\tau(W)$, which if exists is expected to be close in the two channels, and exaggerate the τ_2 error. The $\delta\tau_2$ is seen to correlate with W , with a trend of $\delta\tau_2 \sim -1.5 \times 10^{-2}$ when W increases from 0–6 g cm^{-2} . This small change in τ_2 turns out to be enough to cause a $\delta\alpha \sim -0.5$ trend. These trends are believed to be artifacts of retrievals.

8. Effect of cloud screening and sampling on aerosol retrievals

Aerosol retrievals are made from cloud-free, low-radiance pixels, which remain after removal of bright cloudy pixels. Even small differences in cloud-screening procedure may lead to noticeable effects on aerosol retrievals (cf. analyses of section 7c). Likewise, different sampling may also affect aerosol retrievals. These sources of uncertainty are not easy to quantify, as cloud clearing and/or sampling procedures are typically a complicated set of interdependent tests, consisting of decision trees and many built-in empirical thresholds. The PATMOS and AEROBS data are obtained from the same AVHRR input radiances, but are processed with different cloud screening and sampling procedures. Both use state-of-the-art, peer-reviewed techniques for clear/cloud discrimination with a set of sophisticated tests based upon contrast, spectral and spatial signatures. However, the number and sequence of the tests are different, as well as are the specific thresholds used in the tests. In this section we evaluate the effect of different cloud masks and sampling techniques in AEROBS and PATMOS on aerosol retrievals.

Cloud clearing used in the operational AEROBS files is documented in McClain (1989), with later refinements (mainly related to the use of the high-resolution infrared sounder, HIRS/2 for cloud screening) mentioned in Walton et al. (1998). In PATMOS processing, the Clouds from AVHRR (CLAVR) algorithm was utilized, based solely upon AVHRR measurements (Stowe et al. 1999).

Sampling in AEROBS and PATMOS is also different. All GAC pixels identified by CLAVR as clear are utilized to calculate the PATMOS $(110 \text{ km})^2$ cloud-free statistics. AEROBS processing is done within a window of 11×11 GAC pixels (J. Sapper 2001, personal communication). First, a central array of 2×2 GAC pixels is examined. If all four pixels are cloudy, the algorithm moves on to an adjacent 2×2 array within the same 11×11 window. The algorithm keeps checking the 2×2 arrays until the one is found with cloud-free GAC pixel(s) ($n = 1$ to 4). The n reflectances and brightness temperatures, and aerosol/SST retrievals therefrom, get averaged, along with their respective latitude/longitude and sun-view angles, and recorded to the AEROBS file.

This average (over n GAC pixels; the number n is not saved) record is referred to as an “AEROBS pixel.” Over a low-contrast open ocean (the vast majority of PATMOS–BUOY points pertain to open ocean), the algorithm moves on to a next 11×11 window, until all the globe is covered in along-track increments of 11 and/or cross-track increments of 6 GAC pixels. In certain contrast (coastal) areas, the algorithm is able to process, and output to AEROBS file, up to 5–8 AEROBS pixels within an 11×11 window. It is important to note that the sequence of the 2×2 arrays being tested within an 11×11 window is not fully “blind.” It is designed in such a way that it tends to choose the warmest GAC pixels in the window.

As a result of different scene identification and sampling, different pixels are sampled in AEROBS and PATMOS files. In this section, the effect of these differences on aerosol retrievals is quantified, using one full day of NOAA-14 PATMOS (not restricted to PATMOS–BUOY locations) and AEROBS data obtained on 8 February 1998, within a zonal belt between 5° and 45° S. Both datasets are calibrated using the same calibration (Rao and Chen 1999).

Both datasets contain geo-referenced radiances and sun-view geometry, which are averaged in space: in PATMOS, within the $(110 \text{ km})^2$ grid cells; in AEROBS, over 1 to 4 GAC pixels $[\sim(8 \text{ km})^2]$. On 8 February 1998, PATMOS identifies only 2677 clear-ocean cells in a spatial domain of 5° – 45° S (out of total of 13 039 PATMOS grid cells, of which some are land and some are cloudy), whereas AEROBS identifies 11 797 $\sim(8 \text{ km})^2$ pixels (as mentioned before, the number of original GAC pixels is unknown, but it would be a factor of 1–4 that of AEROBS pixels). For the purpose of further comparison, the AEROBS data have been mapped into PATMOS cells, and their statistics saved. A total of 2409 ocean cells were found, populated with at least one cloud-free AEROBS pixel. Figure 17a plots a histogram of the number of GAC pixels within the 2667 PATMOS cells, and Fig. 17b shows number of AEROBS pixels within the 2409 cells. Figure 17c compares number of GAC pixels in PATMOS data, N_p , with the number of AEROBS pixels, N_A . A difference of up to a factor of ~ 66 (1 AEROBS pixel represents $\frac{1}{2}$ of the 11×11 window, due to the 6-pixel increment in the cross-track direction) is expected, in qualitative agreement with Fig. 17c.

After merging the two, one finds 1850 cells in which both PATMOS and AEROBS data are present. In 1827 PATMOS cells, AEROBS data are missing, and in 559 cells populated with AEROBS data, PATMOS data are not present. This illustrates the difference in sampling resulting from different cloud clearing in the two data sets. In what follows, only the merged dataset ($N = 1850$) is analyzed.

PATMOS reflectances in Fig. 18 are highly correlated with their AEROBS counterparts in both channels ($R^2 \sim 0.93$ – 0.97), but are biased low: The regression inter-

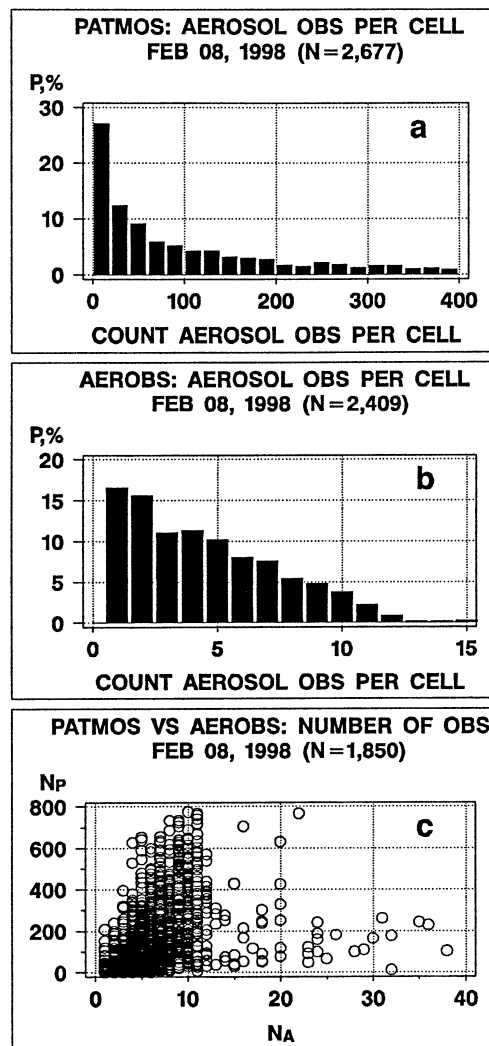


FIG. 17. Histograms of number of cloud-free observations per PATMOS grid cell in (a) PATMOS and (b) AEROBS, and (c) correlation between the two. Data are obtained from NOAA-14 on 18 Feb 1998, in a global latitudinal belt 5° – 45° S.

cepts are negative, and the slopes are less than unity. This implies that CLAVR cloud screening is more conservative compared to the algorithm used in AEROBS. As a result, both τ_{1P} and τ_{2P} in Figs. 19a and 19b are biased low, both additively and multiplicatively. The correlation between the PATMOS and AEROBS τ ($R^2 \sim 0.87$ – 0.89) is somewhat less than that for reflectances, and the rms difference (rmsd) in AOD is $\sigma_\tau \sim 0.02$. The PATMOS/AEROBS differences in the sun and view zenith, and relative azimuth angle data (not shown) contribute to the lesser correlation in τ , compared to ρ . But the primary reason is decreased signal-to-noise ratio in the aerosol component of radiance, ρ^A , which is calculated by subtracting the Rayleigh component from the total reflectance. The PATMOS/AEROBS differences in τ are further evident when the Ångström exponent α is

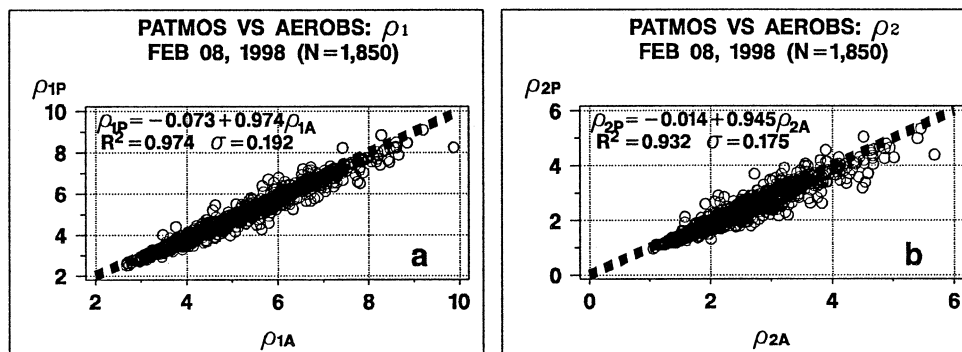


FIG. 18. Correlation between PATMOS (subscript “P”) and AEROS (subscript “A”) reflectances in AVHRR channels (a) 1 and (b) 2. Regression statistics superimposed. Data same as that in Fig. 17.

calculated. The correlation drops to $R^2 \sim 0.55$, with rmsd $\sigma_\alpha \sim 0.3$. Fig. 20 illustrates that scatter in both PATMOS (Fig. 20a) and AEROS (Fig. 20b) α increases toward low τ , as well as scatter in their difference (Fig. 20c). The increased α errors at low τ have been analyzed in detail in section 6. However, a new observation that emerges from Fig. 20 is a relatively lower noise in AEROS data (Fig. 20b) compared to PATMOS (Fig. 20a), despite CLAVR’s seemingly more conservative nature, and larger sample sizes. This observation may help explain the smaller-than-expected increase of the SNR in PATMOS α compared to AEROS in section 6.

Analyses in this section suggest that cloud clearing and sampling may have a noticeable, and difficult to predict, effect on aerosol retrievals. Recall that two state-of-the-art procedures have been consistently applied here to the same input data (reflectances and geometries). Larger errors can be expected when less accurate cloud screening and less sophisticated sampling strategies are used, or when data from different satellite radiometers (such as in Ignatov et al. 2002) are compared.

9. Conclusions

Aerosol optical depths, τ_1 and τ_2 , were derived by two independent, single-channel look-up-tables from 8-yr, two-satellite (1990–93, *NOAA-11*; and 1995–98, *NOAA-14*) Pathfinder Atmosphere AVHRR reflectances in channels 1 ($0.63 \mu\text{m}$) and 2 ($0.83 \mu\text{m}$) merged with Pathfinder Oceans Matchup Buoy Database buoy observations (PATMOS–BUOY). The retrievals of τ_1 and τ_2 , and derived Ångström exponent α have been examined empirically to see if they are physically realistic and self-consistent, before their application in deriving the NOAA/NESDIS Phase II aerosol SST correction to be described in a companion paper.

Retrievals at solar zenith angles $\theta_o > 60^\circ$ were biased low, suggesting removal of $\Delta N_s = 18\,585$ data points ($\sim 17.6\%$) from subsequent analyses. The remaining N

$= 87\,246$ data points were further screened for outliers using a set of quality control procedures, which removed $\Delta N_{\text{QC}} = 330$ ($\sim 0.4\%$) data points. The remaining analyses were done with the quality-controlled data ($N = 86\,916$).

Histograms of τ were accurately represented by log-normal probability density functions (PDFs), with global 8-yr (1990–93, 1995–98) geometrical means of $\tau_{g1} = 0.126$, $\tau_{g2} = 0.117$, and geometrical standard deviations of $\mu_1 \sim \mu_2 \sim 1.8$ (see section 5a for definitions). For a 5-yr period of 1990, 1995–98, excluding the Mt. Pinatubo-contaminated portion of *NOAA-11*, the estimates were $\tau_{g1} = 0.113$, $\tau_{g2} = 0.106$, $\mu_1 \sim \mu_2 \sim 1.7$. The latter numbers can be considered representative of typical global climatological statistics of τ_1 and τ_2 . The retrieved Ångström exponent was accurately fit by a normal PDF. Estimate of its true statistic, however, was not straightforward, due to a sizeable retrieval error contribution.

The τ_1 – τ_2 scattergram converged at the origin as expected, but it was shifted with respect to its expected domain, defined by two straight lines corresponding to $\alpha = 0$ and $\alpha = 2$, thus resulting in a negative bias in α . These results, consistent with observations by Ignatov and Stowe (2002b) made from AEROS data, call for an adjustment to the current model water vapor absorption in AVHRR channel 2, as predicted with the 6S radiative transfer model.

Special statistical analyses with τ_1 – τ_2 and α – τ scattergrams were aimed at separating signal from noise in the retrievals. The α – τ scattergram showed increased scatter, in inverse proportion to τ , but no systematic $1/\tau$ trend in α . The rms error in α was approximated as $\sigma_{\alpha\epsilon}/\tau_1$, with $\sigma_{\alpha\epsilon} \sim 0.032$ (cf. $\sigma_{\alpha\epsilon} \sim 0.042 \pm 0.002$ from AEROS data). The “natural” (noise free; represented with subscript “o”) variability of the Ångström exponent within the PATMOS–BUOY dataset was found to be $\sigma_{\alpha o} \sim 0.30 \pm 0.02$. This number, derived from global maritime multiyear data, was higher than the value of $\sigma_{\alpha o} \sim 0.24 \pm 0.02$ found earlier in the space–time restricted AEROS datasets. The cross-over point in τ at

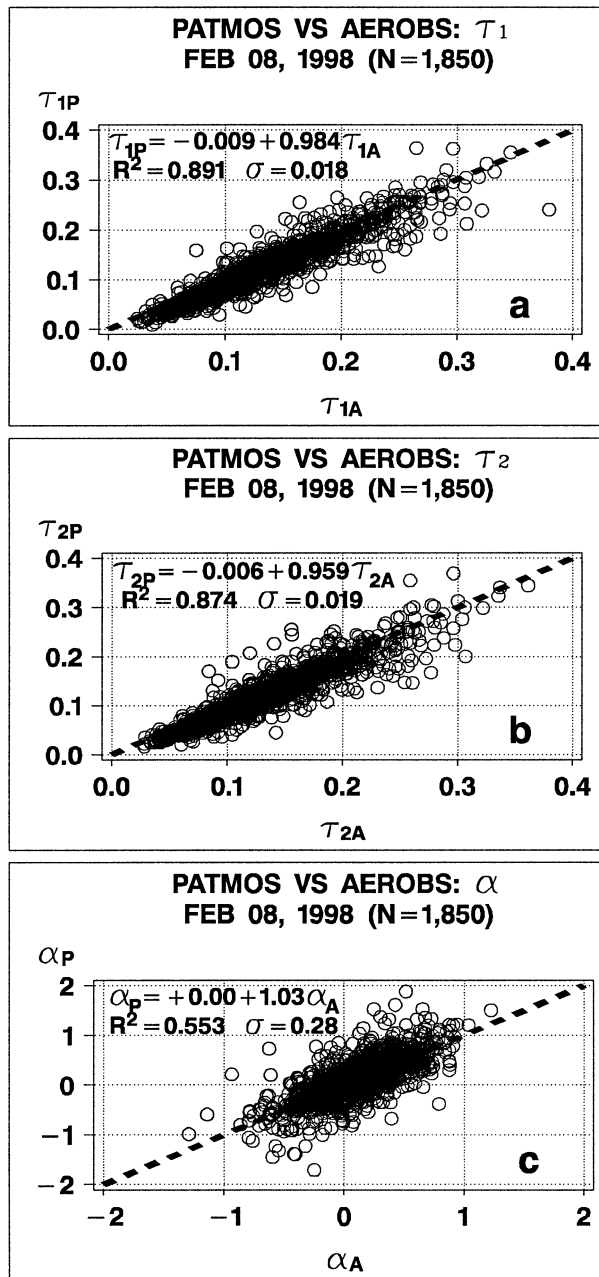


FIG. 19. Same as in Fig. 18, but for aerosol retrievals of (a) τ_1 , (b) τ_2 , and (c) α .

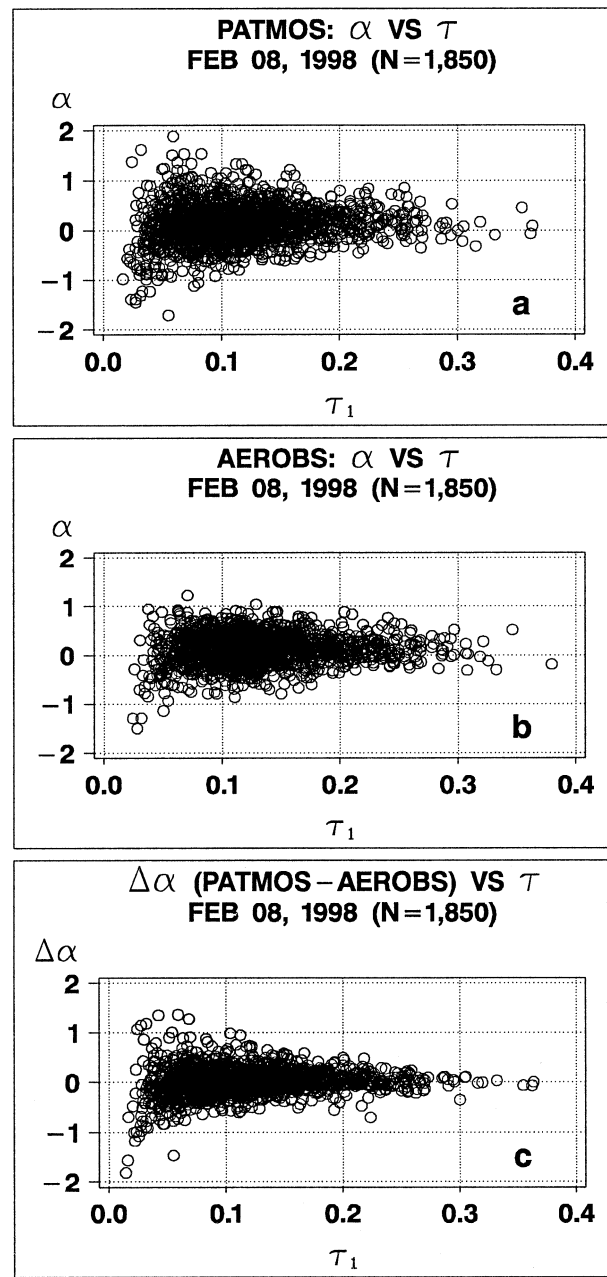


FIG. 20. Scattergrams of α vs τ_1 in (a) PATMOS and (b) AEROBS data averaged over PATMOS grid cells, and (c) their difference (PATMOS-AEROBS) $\Delta\alpha$.

which the signal-to-noise ratio in the Ångström exponent, defined as $\eta = (\sigma_{ao}/\sigma_{ae})\tau_1 \sim \tau_1/\tau_{10}$ becomes 1 was found to be at $\tau_{10} \sim 0.11 \pm 0.01$ (cf. $\tau_{10} \sim 0.18 \pm 0.02$ estimated from AEROBS data). For reference, the Phase I aerosol SST correction is applied only when $\tau_1 > 0.15$ (Nalli and Stowe 2002).

Trend analyses revealed a number of observations. For both NOAA-11 and -14, τ_1 and τ_2 increased by about +0.02 to +0.03 over a period of 4 years. For NOAA-14, the trends were largely coherent in the two channels,

contributing to a more stable Ångström exponent. For NOAA-11, however, the Ångström exponent declined by ~ 0.4 . These time trends most probably resulted from the remaining calibration uncertainties. Geographical trends were largely consistent with the known distribution of aerosol parameters but showed zonal correlation with cloud amount. The latter observation was confirmed by direct correlation analyses of aerosol retrievals (made from a cloud-free portion of a PATMOS

grid cell) with the average ambient cloud amount within a cell. Additional PATMOS/AEROBS comparisons revealed large sensitivity of aerosol retrievals to cloud screening and sampling. The retrievals also showed some statistically significant angular trends in the mean values of τ and α , but not in τ_{\min} , which may be attributed to the remaining minor aerosol retrieval model inadequacies and/or sampling biases. The surface wind speed trends in aerosol retrievals are in a qualitative agreement with those observed in sun photometer data. Water vapor trends are small in τ_1 , but statistically significant in τ_2 and α . The water vapor trends, and a part of wind speed trends, may be artifacts of the retrieval algorithm, which used assumptions of a constant surface diffuse reflectance, surface wind speed and water vapor concentration in the retrievals. We recommend that these parameters be added to the PATMOS and AEROBS files. Despite these remaining problems, the retrievals are largely self- and interconsistent, and should provide a superior set of predictors for the NOAA/NESDIS Phase II aerosol SST correction.

Acknowledgments. We are greatly indebted to Larry Stowe (retired) and Nagaraja Rao (deceased) who initiated the program in aerosol remote sensing applications from AVHRR at NESDIS. Their prior contributions were indispensable. We are also grateful to John Sapper, Alexander Smirnov, Dmitry Kabanov, Sergey Sakerin, Andrew Harris, Istvan Laszlo, and Larry Flynn for helpful comments and advice. Comprehensive reviews and constructive to-the-point comments from Oleg Dubovik and an anonymous reviewer were very helpful for revising the manuscript, and are greatly acknowledged. This project was funded under the NOAA/NESDIS Ocean Remote Sensing and NASA EOS/CE-RES Programs. We are thankful to Bill Pichel, Al Strong, Bruce Wielicki, and Bruce Barkstrom for support and encouragement.

REFERENCES

- Dubovik, O., and M. King, 2000: A flexible inversion algorithm for retrieval of aerosol optical properties from sun and sky radiance measurements. *J. Geophys. Res.*, **105**, 20 673–20 696.
- , T. Lapyonok, and S. Oshchepkov, 1995: Improved technique for data inversion: Optical sizing of multicomponent aerosols. *Appl. Opt.*, **34**, 8422–8436.
- Edie, W., T. Dryard, F. James, M. Roos, and B. Sadoulet, 1971: *Statistical Methods in Experimental Physics*. North-Holland, 155 pp.
- Higurashi, A., and T. Nakajima, 1999: Development of a two-channel aerosol retrieval algorithm on a global scale using NOAA/AVHRR. *J. Atmos. Sci.*, **56**, 924–941.
- Ignatov, A., 2002: Sensitivity and information content of aerosol retrievals from AVHRR: Radiometric factors. *Appl. Opt.*, **41**, 991–1011.
- , and L. Stowe, 2000: Physical basis, premises, and self-consistency checks of aerosol retrievals from TRMM VIRS. *J. Appl. Meteor.*, **39**, 2259–2277.
- , and —, 2002a: Aerosol retrievals from individual AVHRR channels. Part I: Retrieval algorithm, and transition from Dave to 6S radiative transfer model. *J. Atmos. Sci.*, **59**, 313–334.
- , and —, 2002b: Aerosol retrievals from individual AVHRR channels. Part II: Quality control, probability distribution functions, and consistency checks of retrievals. *J. Atmos. Sci.*, **59**, 335–362.
- , —, and R. Singh, 1998: Sensitivity study of the Ångström exponent derived from AVHRR over oceans. *Adv. Space Res.*, **21**, 439–442.
- , I. Laszlo, and N. Nalli, 2002: Statistical patterns in aerosol retrievals from NOAA/AVHRR and TRMM/VIRS. Preprints, *11th Conf. on Atmospheric Radiation*, Ogden, UT, Amer. Meteor. Soc., CD-ROM, 5.3.
- Kabanov, D., and S. Sakerin, 2000: Transmission of the atmosphere over the Atlantic Ocean 2. Variations of the aerosol optical thickness and moisture content. *Atmos. Oceanic Opt.*, **13**, 664–670.
- Kidwell, K., 1995: NOAA polar orbiter data user's guide. National Environmental Satellite Data and Information Service, National Oceanic and Atmospheric Administration, U.S. Dept. of Commerce, 394 pp. [Available from NOAA Satellite Data Services Division, Federal Office Building #3, Room G233, Washington, DC 20233.]
- Kilpatrick, K., G. Podesta, and R. Evans, 2001: Overview of the NOAA/NASA AVHRR Pathfinder algorithm for sea surface temperature and associated matchup database. *J. Geophys. Res.*, **106**, 9179–9197.
- McClain, E. P., 1989: Global SST and cloud clearing for aerosol optical depth estimates. *Int. J. Remote Sens.*, **10**, 763–769.
- Mishchenko, M. I., I. V. Geogdzhayev, B. Cairns, W. B. Rossow, and A. Lacis, 1999: Aerosol retrievals over the oceans by use of channels 1 and 2 AVHRR data: Sensitivity analysis and preliminary results. *Appl. Opt.*, **38**, 7325–7341.
- Nalli, N. R., and L. L. Stowe, 2002: Aerosol correction for remotely sensed sea surface temperatures from the NOAA AVHRR. *J. Geophys. Res.*, in press.
- O'Neill, N. T., A. Ignatov, B. Holben, and T. Eck, 2000: The log-normal distribution as a reference for reporting aerosol optical depth statistics: Empirical tests using multi-year, multi-site AERONET sun photometer data. *Geophys. Res. Lett.*, **27**, 3333–3336.
- Platt, C., and G. Patterson, 1986: The interpretation of baseline atmospheric turbidity measurements at Cape Grim, Tasmania. *J. Atmos. Chem.*, **4**, 187–197.
- Rao, N., and J. Chen, 1999: Revised post-launch calibration of the visible and near-infrared channels of the advanced very high resolution radiometer (AVHRR) on the NOAA-14 spacecraft. *Int. J. Remote Sens.*, **20**, 3485–3491.
- Smirnov, A., Y. Villevalde, N. O'Neill, A. Royer, and A. Tarusov, 1995: Aerosol optical depth over the oceans: Analysis in terms of synoptic air mass types. *J. Geophys. Res.*, **100** (D8), 16 639–16 650.
- Stowe, L., A. Ignatov, and R. Singh, 1997: Development, validation and potential enhancements to the second generation operational aerosol product at NOAA/NESDIS. *J. Geophys. Res.*, **102**, 16 923–16 934.
- , P. Davis, and P. McClain, 1999: Scientific basis and initial evaluation of the CLAVR-1 global clear/cloud classification algorithm for the Advanced Very High Resolution Radiometer. *J. Atmos. Oceanic Technol.*, **16**, 656–681.
- , H. Jacobowitz, G. Ohring, K. Knapp, and N. Nalli, 2002: The Advanced Very High Resolution Radiometer Pathfinder Atmosphere (PATMOS) climate dataset: Initial analyses and evaluations. *J. Climate*, **15**, 1243–1260.
- Tanre, D., Y. J. Kaufman, M. Herman, and S. Mattoo, 1997: Remote sensing of aerosol properties over oceans using the MODIS/EOS spectral radiances. *J. Geophys. Res.*, **102**, 16 971–16 988.
- Tarantola, A., 1987: *Inverse Problem Theory: Methods for Data Fitting and Model Parameters Estimation*. Elsevier, 500 pp.
- Teillet, P., 1990: Rayleigh optical depth comparisons from various sources. *Appl. Opt.*, **29**, 1897–1900.

- Vermote, E., D. Tanre, J. L. Deuze, M. Herman, and J. J. Morcrette, 1997: Second simulation of the satellite signal in the solar spectrum, "6S": An overview. *IEEE Trans. Geosci. Remote Sens.*, **35**, 675–686.
- Wagner, R., S. Nemesure, and S. E. Schwartz, 1997: Aerosol optical depth over oceans: High space- and time-resolution retrieval and error budget from satellite radiometry. *J. Atmos. Oceanic Technol.*, **14**, 577–590.
- Walton, C., W. Pichel, J. Sapper, and D. May, 1998: The development and operational application of nonlinear algorithms for the measurement of sea surface temperatures with the NOAA polar orbiting environmental satellites. *J. Geophys. Res.*, **103**, 27 999–28 012.
- Wilson, S., and B. Forgan, 2002: Aerosol optical depth at Cap Grim, Tasmania, 1986–1999. *J. Geophys. Res.*, **107** (D8), AAC6.1–6.8.